

The observation of quantum fluctuations in a kagome Heisenberg antiferromagnet

Fangjun Lu,^{1,*} Long Yuan,^{1,*} Jian Zhang,¹ Boqiang Li,¹ Yongkang Luo,^{1,†} and Yuesheng Li^{1,‡}

¹Wuhan National High Magnetic Field Center and School of Physics,
Huazhong University of Science and Technology, 430074 Wuhan, China

(Dated: October 25, 2022)

Abstract

The search for the experimental evidence of quantum spin liquid (QSL) states is critical but extremely challenging, as the quenched interaction randomness introduced by structural imperfection is usually inevitable in real materials. $\text{YCu}_3(\text{OH})_{6.5}\text{Br}_{2.5}$ (YCOB) is a spin-1/2 kagome Heisenberg antiferromagnet (KHA) with strong coupling of $\langle J_1 \rangle \sim 51$ K but without conventional magnetic freezing down to 50 mK $\sim 0.001\langle J_1 \rangle$. Here, we report a Br nuclear magnetic resonance (NMR) study of the local spin susceptibility and dynamics on the single crystal of YCOB. The temperature dependence of NMR main-line shifts and broadening can be well understood within the frame of the KHA model with randomly distributed hexagons of alternate exchanges, compatible with the formation of a randomness-induced QSL state at low temperatures. The in-plane spin fluctuations as measured by the spin-lattice relaxation rates ($1/T_1$) exhibit a weak temperature dependence down to $T \sim 0.03\langle J_1 \rangle$. Our results demonstrate that the majority of spins remain highly fluctuating at low temperatures despite the quenched disorder in YCOB.

Introduction

Quantum spin liquid (QSL) is a state of matter that exhibits exotic fractional excitations and long-range entanglement without symmetry breaking [1–4]. Since Anderson’s proposal of the prototype, i.e., resonating-valence-bond (RVB) state, in 1973 [5], QSL has been attracting researchers for decades, due to its key role in understanding high-temperature superconductivity [6] and the possible realization of the topological quantum computation [7]. Experimentally, many prominent two-dimensional QSL candidate compounds have been extensively studied (the one-dimensional scenario of QSL is qualitatively different [2]), including the kagome-lattice $\text{ZnCu}_3(\text{OH})_6\text{Cl}_2$ (herbertsmithite) [8–17], triangular-lattice $\kappa\text{-(ET)}_2\text{Cu}_2(\text{CN})_3$ [18, 19], $\text{EtMe}_3\text{Sb}[\text{Pd}(\text{dmit})_2]_2$ [20, 21], YbMgGaO_4 [22, 23], etc., all of which generally exhibit gapless QSL behaviors [9, 11, 14, 16, 18–20, 22, 24–27], but without evident magnetic thermal conductivity [28–32].

Despite the progress, the existing experimental evidence for QSL remains circumstantial and strongly depends on theoretical interpretation. The root cause lies in the quenched interaction randomness introduced by structural imperfection that is inevitable in all real materials [2, 17, 33]. Therefore, great efforts are being devoted to exploring for ultrahigh-quality candidate materials, which is extremely challenging [2]. On the other hand, disorder-free QSL, even if successfully pre-

pared, is usually very fragile. For instance, the most frustrated kagome Heisenberg antiferromagnet (KHA) falls back to conventional long-range magnetic ordering in the presence of a weak next-nearest-neighbor coupling $|J_2| \geq 0.03J_1$ [34] or Dzyaloshinsky-Moriya interaction $|D| \geq 0.012J_1$ [35]. These constrictions further compress the “living space” of disorder-free perfect QSL compounds.

Alternatively but more realistically, one could first find out whether the inherent randomness is fatal or vital to the QSL physics [4]. In fact, this same question can also be raised for high-temperature superconductivity, as it is generally believed that Cooper pairs naturally form once the RVB states are charged upon chemical doping [6, 36]. The presence of quenched vacancies in the KHA can lead to a valence bond glass ground state (GS) [37]. Further, Kawamura et al. found that randomness-induced QSL GSs instead of spin glasses form in both KHA and triangular Heisenberg antiferromagnet with strong bond randomness, $\Delta J/J_1 \geq 0.4$ and 0.6 [38, 39], respectively, which may explain the gapless behaviors observed in $\text{ZnCu}_3(\text{OH})_6\text{Cl}_2$, $\kappa\text{-(ET)}_2\text{Cu}_2(\text{CN})_3$, $\text{EtMe}_3\text{Sb}[\text{Pd}(\text{dmit})_2]_2$ [33], etc. Later similar scenarios have been generally applied to the gapless QSL behaviors observed in the strongly-spin-orbital-coupled triangular-lattice YbMgGaO_4 [40, 41] with the mixing of $\text{Mg}^{2+}/\text{Ga}^{3+}$ [26, 42], as well as in other relevant materials [43]. Despite the growing interest in theory, the key issue is whether the paramagnetic phase conspired by frustration and randomness in real materials is relevant to the exotic QSL/RVB state with strong quantum fluctuations, or simply a trivial product state of quenched random singlets. To address this issue, local and dynamic measurements on QSL candidates with quantifiable randomness are particularly needed.

Recently, a $S = 1/2$ KHA $\text{YCu}_3(\text{OH})_{6.5}\text{Br}_{2.5}$ (YCOB) has been proposed, without any global symmetry reduction of the kagome lattice (space group $P\bar{3}m1$, see Fig. 1d) [44–46]. Neither long-range magnetic ordering nor spin-glass freezing was observed down to 50 mK $\sim 0.001\langle J_1 \rangle$, as evidenced by specific heat [46], thermal conductivity [47], and ac susceptibility [44, 45] measurements. The observed power-law T dependence of low- T specific heat suggests the appearance of gapless spin excitations [44, 46]. Unlike other known QSL materials (e.g. $\text{ZnCu}_3(\text{OH})_6\text{Cl}_2$ [14–16, 48, 49]), the mixing between Cu^{2+} and other nonmagnetic ions is prohibited due to the significant ionic difference, thus defect orphan spins are essentially negligible [44]. Further, the antisite mixing of the polar OH^- and nonpolar Br^- causes 70(2)% of randomly distributed hexagons of alternate exchanges (e.g. Fig. 1b) on the kagome lattice (Fig. 1d), which accounts for the measured

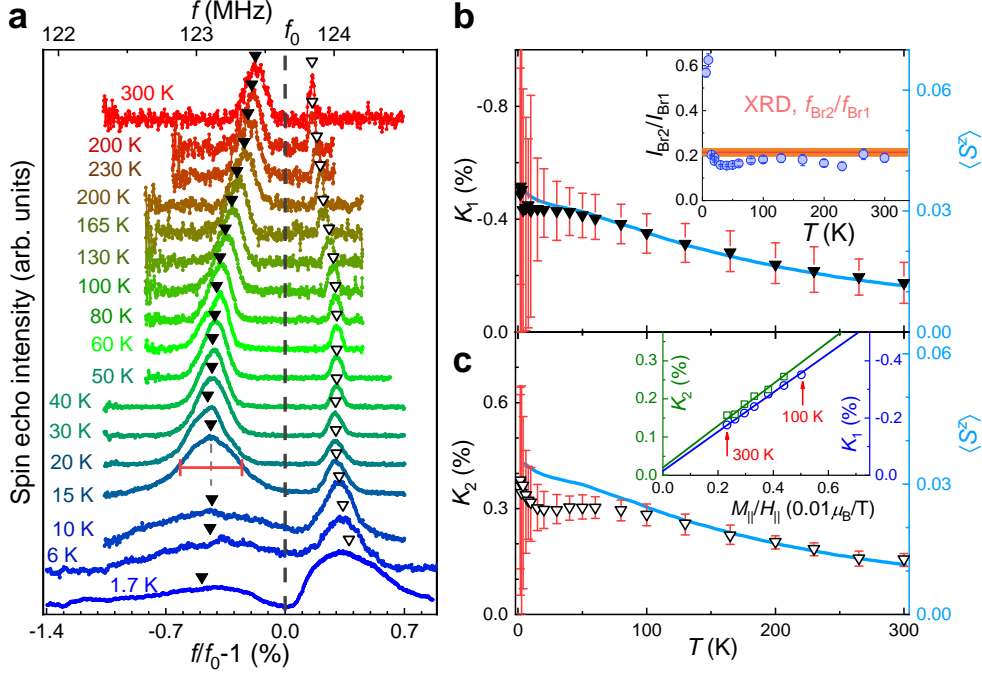


FIG. 2. **Nuclear magnetic resonance spectra of $\text{YCu}_3(\text{OH})_{6.5}\text{Br}_{2.5}$.** (a) Frequency-sweep spectra measured on the sample S_1 at a field $\mu_0 H_{\parallel} \sim 10.75$ T (the reference frequency $f_0 = {}^{81}\gamma_n \mu_0 H_{\parallel} \sim 123.64$ MHz). The shifts of two lines, K_1 and K_2 , are marked by solid and hollow triangles, respectively. Temperature dependence of K_1 (b) and K_2 (c), with the bulk magnetization ($\langle S^z \rangle$) measured at $\mu_0 H_{\parallel} = 10.75$ T for comparison. The inset of b shows the ratio between the integrated intensities of ${}^{81}\text{Br}2$ and ${}^{81}\text{Br}1$ lines ($I_{\text{Br}2}/I_{\text{Br}1}$), as well as the stoichiometric ratio from x-ray diffraction [44]. Inset of c displays K_1 and K_2 shifts vs bulk susceptibility χ_{\parallel} (i.e. $M_{\parallel}/H_{\parallel}$). The red bars display the normalized frequency regions where the intensity is larger than half of the maximum value in b and c, and error bars on $I_{\text{Br}2}/I_{\text{Br}1}$ show a standard error from the fit.

significant (see Fig. 2) and the calculated local magnetization is nearly spatially homogeneous (see Fig. 3a), and thus one expects a scaling law $K = A_{\text{hf}}\chi_{\parallel} + K_0$, where A_{hf} presents the hyperfine coupling between Br (Br1 or Br2) nuclear and Cu^{2+} electronic spins. By fitting the experimental data (see inset of Fig. 2c), we obtain $A_{\text{hf}1} = -0.68(2)$ T/ μ_B , $K_{01} = -0.015(7)\%$ and $A_{\text{hf}2} = 0.55(3)$ T/ μ_B , $K_{02} = 0.02(1)\%$. The presence of both negative and positive hyperfine couplings of the same nuclear species is surprising, and the underlying mechanism must be complex, including both the positive and negative contributions.

The NMR shift of Br2 probes spins of hexagons on the kagome lattice (Fig. 1b,c), but is obviously smaller than $A_{\text{hf}2}\chi_{\parallel}$ ($K_{02} \ll K_2$) below 100 K (Fig. 2c). In fact, the formation energy of the optimized nonsymmetric Br2-OH2 stacking sequence (Fig. 1b) (-37.8 eV/FU), is $\sim 2.5 \times 10^4$ K/FU lower than that of the symmetric Br2-Br2 configuration (Fig. 1c) (-35.7 eV/FU). Therefore, Br2 ions actually prefer the nonsymmetric local environments, and Br2 nuclear spins mainly probe the nonsymmetric hexagons with alternate exchanges [44] ($J_{1a} > J_{1c}$) as illustrated in Fig. 1b. Intuitively, the nonsymmetric hexagon tends to locally release the frustration and form three nonmagnetic singlets along the stronger couplings J_{1a} (see Fig. 3e), which accounts for the relatively smaller Br2 shifts observed below 100 K (Fig. 3a). More-

over, the Br1 line detects the site susceptibility/magnetization of all the Cu^{2+} spins with exchange couplings J_{1a} , J_{1b} , and J_{1c} , whereas the Br2 line mainly probes the hexagons of spins only with J_{1a} and J_{1c} . The Br2 line probes less kinds of Cu^{2+} spins, and thus is narrower than the Br1 line.

Quantitatively, the temperature dependence of both Br1 and Br2 shifts can be reproduced by the average magnetization of all the triangles and nonsymmetric hexagons on the kagome lattice, viz. $K_1 \sim A_{\text{hf}1} g_{\parallel} \overline{\langle S^z \rangle} / (\mu_0 H_{\parallel})$ and $K_2 \sim A_{\text{hf}2} g_{\parallel} \overline{\langle S^z_{\text{nh}} \rangle} / (\mu_0 H_{\parallel})$, respectively (see Fig. 3a), with $J_{1a} = 89$ K, $J_{1b} = 48$ K, and $J_{1c} = 16$ K ($\langle J_1 \rangle \sim 51$ K) experimentally determined by bulk susceptibilities (Supplementary Note 1 and Supplementary Fig. 2). Taking all the triangles and nonsymmetric hexagons into account, we are able to simulate the broadening of both Br1 and Br2 lines by introducing the distributed density $\propto dn_S(\langle S^z \rangle) / d\langle S^z \rangle$ (see Fig. 3b,c), where $dn_S(\langle S^z \rangle)$ is the number of triangles or nonsymmetric hexagons with the local magnetization (per site) ranging from $\langle S^z \rangle$ to $\langle S^z \rangle + d\langle S^z \rangle$. $\langle S^z \rangle$ is thermally averaged, so the distributed density is a function of T .

The simulations also enable us to revisit the correlation functions $\langle \mathbf{S}_i \cdot \mathbf{S}_j \rangle$ in this KHA system with randomness. Compared to the ideal case (Fig. 3f), a small fraction ($\sim 3/54$) of well-defined singlets with $\langle \mathbf{S}_i \cdot \mathbf{S}_j \rangle \sim -0.7 \rightarrow -0.75$ are frozen

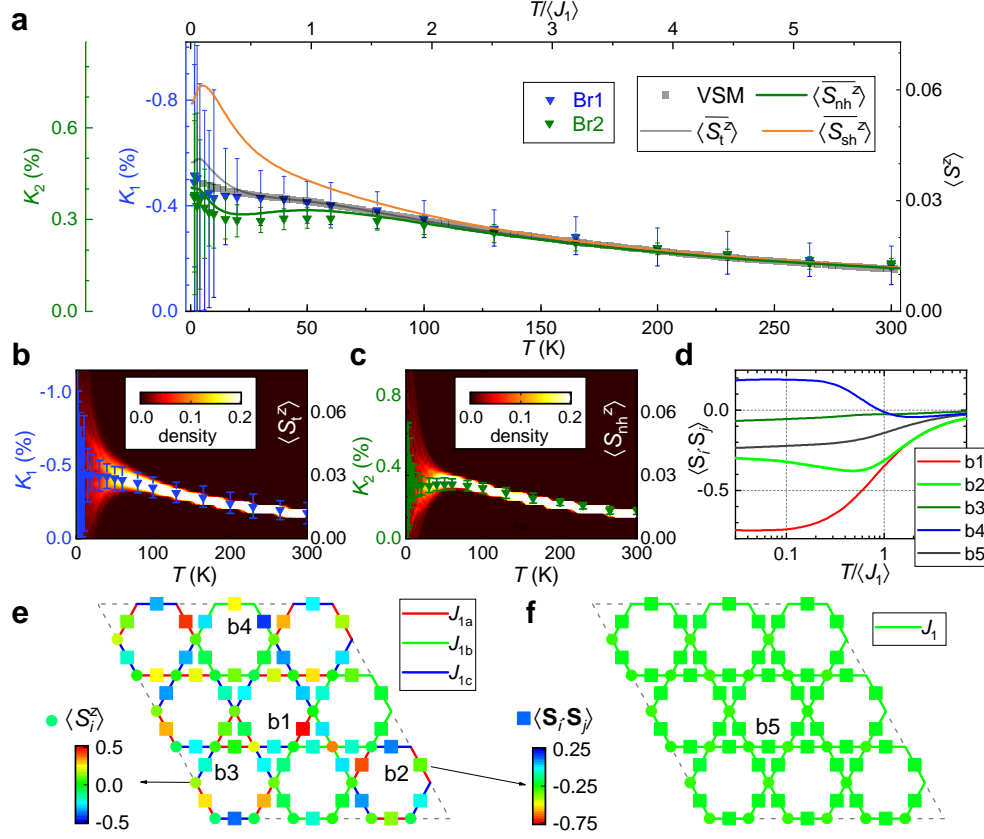


FIG. 3. **Simulations of the spatially inhomogeneous susceptibility probed by nuclear magnetic resonance (NMR) spectra.** (a) Temperature dependence of NMR shifts K_1 and K_2 , as well as bulk $\langle S^z \rangle$ measured in a vibrating sample magnetometer at a field $\mu_0 H_{\parallel} = 10.75$ T. The colored lines show the calculated average $\langle S^z \rangle$ over all the triangles ($\langle S_t^z \rangle$), nonsymmetric hexagons ($\langle S_{nh}^z \rangle$), and symmetric hexagons ($\langle S_{sh}^z \rangle$). (b,c) The finite-temperature Lanczos diagonalization results of local magnetization of triangles ($\langle S_t^z \rangle$) and nonsymmetric hexagons ($\langle S_{nh}^z \rangle$), along with the measured K_1 and K_2 , respectively. (d) Calculated local correlations of the selected spin pairs (see e,f) as function of normalized temperature $T/\langle J_1 \rangle$ and $\mu_0 H_{\parallel} = 10.75$ T. The solid circles and squares stand for local magnetization $\langle S_i^z \rangle$ at the kagome site i and correlation function $\langle S_i \cdot S_j \rangle$ of the nearest-neighbor spin pair $\langle ij \rangle$, respectively. (f) The same calculations as in e, but within the ideal KHA model. The dashed lines mark the clusters with periodic boundary conditions, and J_{1a} , J_{1b} , J_{1c} , and J_1 present the exchange couplings. The color scale in b and c quantifies the distributed density, whereas the ones in e and f quantify the local magnetization (circles) and correlation function (squares), respectively. The bars in a-c show the regions where the intensities are larger than half of the maximum value.

at low T in YCOB (Fig. 3e), which is a signature of releasing frustration due to the quenched randomness. These local singlets might confine the mobile spinons [27, 37, 51, 52], which might be responsible for the absence of large magnetic thermal conductivity observed in nearly all of the existing gapless QSL candidates, including the well-known $\text{ZnCu}_3(\text{OH})_6\text{Cl}_2$ [28, 29], $\text{EtMe}_3\text{Sb}[\text{Pd}(\text{dmit})_2]_2$ [30, 31], etc. However, the majority of antiferromagnetic interactions remain not fully satisfied at low T (see Fig. 3d,e), and the GS wavefunction should be represented by a superposition of various pairings of spins. It is worth to mention that the weights of different pairings should be different due to the quenched randomness. The survival of strong frustration in the $S = 1/2$ random KHA speaks against the product GS wavefunction of randomly distributed singlets, and may still give rise to strong quantum fluctuations. To testify this, we turn to the spin dy-

namics of YCOB mainly probed by the spin-lattice relaxation rates as follow.

Spin dynamics. The representative spin-lattice relaxation data measured on YCOB are displayed in Figs 4a and 4b, which can be well fitted to the single-exponential function for the central transition of $I = 3/2$ nuclear spins, i.e.,

$$M(t) = M_0 - 2M_0 F \left[\frac{1}{10} e^{-\frac{t}{T_1}} + \frac{9}{10} e^{-\frac{6t}{T_1}} \right], \quad (1)$$

where M_0 and F are scale parameters for intensity. Alternatively, the relaxation data may be fitted with the stretched-exponential one,

$$M(t) = M_0 - 2M_0 F \left[\frac{1}{10} e^{-(\frac{t}{T_1})^\beta} + \frac{9}{10} e^{-(\frac{6t}{T_1})^\beta} \right]. \quad (2)$$

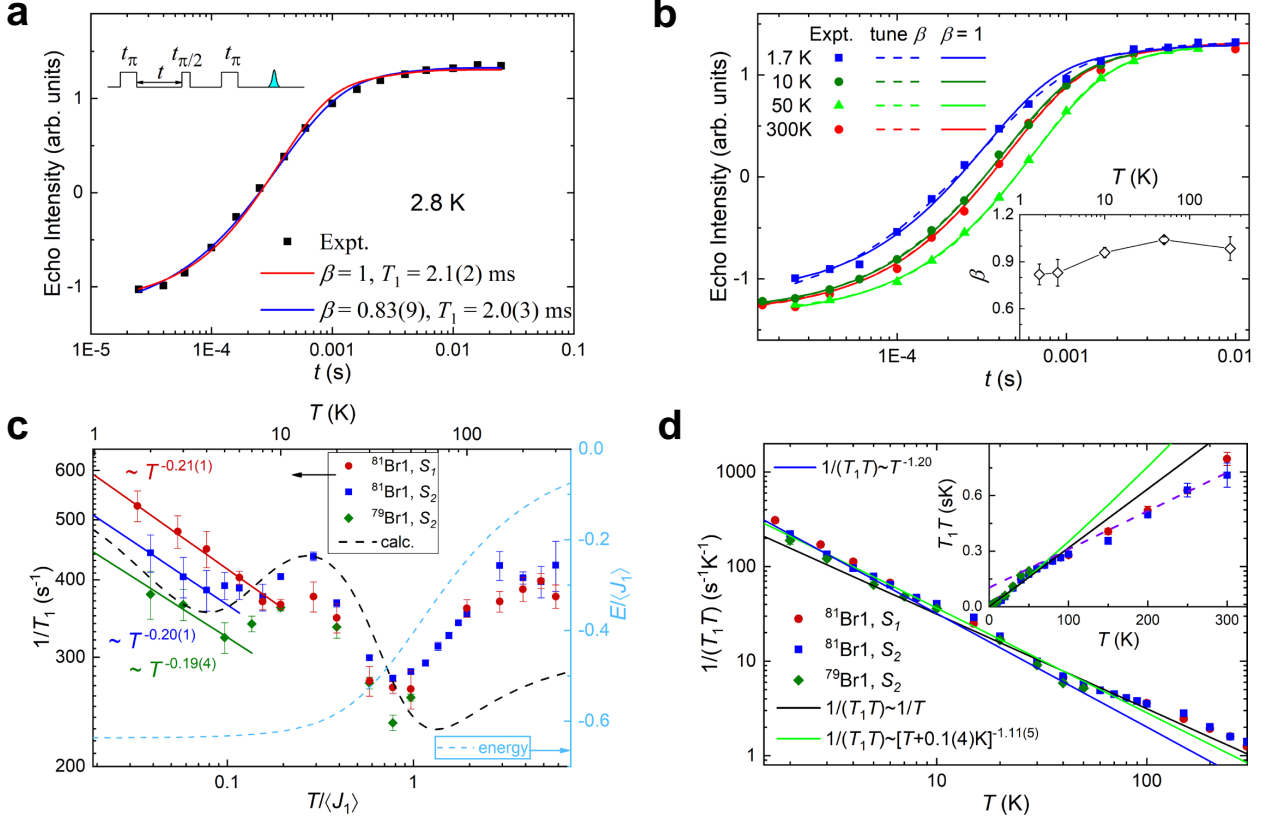


FIG. 4. **Nuclear spin-lattice relaxation of $\text{YCu}_3(\text{OH})_{6.5}\text{Br}_{2.5}$.** (a) A representative $T = 2.8$ K spin-lattice relaxation of Br1 measured by an inversion recovery method, fitted to the stretched-exponential function with fixing $\beta = 1$ (red) and tuning β (blue). The pulse sequence for T_1 measurements is depicted in the inset. (b) The same fits to the relaxation data measured at other selected temperatures. The inset shows the fitted stretching exponent β . (c) Temperature dependence of $^{81}\text{Br}1$ nuclear spin-lattice relaxation rate $1/T_1$ measured on the sample S_1 at a field $\mu_0 H_{\parallel} = 10.75$ T, as well as $^{81}\text{Br}1$ and $^{79}\text{Br}1$ $1/T_1$ measured on S_2 at $\mu_0 H_{\parallel} = 10.75$ and 11.59 T, respectively. The colored lines present the power-law fits to the experimental data below ~ 10 K $\sim 0.2\langle J_1 \rangle$, the dashed black and blue lines are the $1/T_1$ and energy (per site), respectively, calculated by using the random kagome Heisenberg antiferromagnet model of $\text{YCu}_3(\text{OH})_{6.5}\text{Br}_{2.5}$. (d) The Curie ($\sim T^{-1}$, black lines) and critical ($\sim (T - T_c)^{-\alpha' - 1}$, the critical temperature $T_c = -0.1 \pm 0.4$ K, green lines) fits to $1/(T_1 T)$ at $1.7 \leq T \leq 300$ K. The blue line is the low- T power-law dependence as shown in c. The inset shows the $T_1 T$ vs T plot, where the dashed violet line displays the antiferromagnetic Curie-Weiss behavior ($T_1 T \sim T + \langle J_1 \rangle \sim 50$ K). The T_1 data presented in c and d are obtained from the single-exponential fits (i.e., $\beta = 1$, see a and b), and the stretched-exponential fits are made only for comparison in a and b. Error bars on the experimental data points show a standard error from fit, and the error bars in a and b are small.

Here, the stretching exponent β slightly decreases at low temperatures (see inset of Fig. 4b), but remains large down to the lowest temperature of 1.7 K, $\beta > 0.8$. Moreover, the fit to the single T_1 function (i.e. $\beta = 1$) is still good even at 1.7 K (Fig. 4b), with the adj. $R^2 = 0.997$ [53]. The inclusion of the additional fitting parameter β only slightly improves the fit (the adj. R^2 increases to 0.998), and even makes the standard error on T_1 larger. Therefore, all the following T_1 data are obtained with the single-exponential fits.

Figure 4c shows the results of Br1 nuclear spin-lattice relaxation rates ($1/T_1$). Br1 $1/T_1$ is highly sensitive to the electronic spin fluctuations perpendicular to the applied magnetic field on the kagome layer via the hyperfine coupling [39, 54–

56],

$$\frac{1}{T_1} \sim \frac{T}{hf_0} \sum_{\mathbf{q}} \chi''(\mathbf{q}, f_0) \sim \frac{\pi \gamma_n^2 A_{\text{hf1}}^2 g_{\perp}^2}{Z} \sum_{\mathbf{q}, m, m'} e^{-\frac{E_m}{k_B T}} \times |\langle m' | S_{\mathbf{q}}^{\perp} | m \rangle|^2 \delta(f_0 - \frac{E_{m'} - E_m}{h}), \quad (3)$$

where the \mathbf{q} dependence of A_{hf1} is neglected, $f_0 = \gamma_n \mu_0 H_{\parallel} (\ll k_B T/h) \rightarrow 0$ presents the NMR frequency, $S_{\mathbf{q}}^{\perp}$ is the Fourier transform of S_i^{\perp} over all triangles, and $Z = \sum_m \exp(-E_m/k_B T)$ the partition function. In our simulation of $1/T_1$, the delta function is replaced by a Gaussian distribution with narrow width $\sim 10^{-4} \langle J_1 \rangle / h$ [39, 56].

At high temperatures ($T \gg \langle J_1 \rangle$), the Moriya paramagnetic limit yields the T -independent $1/T_1^{\infty} =$

$(2\pi)^{1.5}\gamma_n^2 A_{\text{hf}}^2 g_1^2 S(S+1)/(3z_1\nu_e) \sim 300 \text{ s}^{-1}$, reasonably comparable with the observation (see Fig. 4c), where $\nu_e = \langle J_1 \rangle \sqrt{2zS(S+1)}/3/h$ is the exchange frequency with the coordination number $z = 4$ [55, 57, 58]. Upon cooling, $1/T_1$ slightly decreases first and then rises at $T \sim \langle J_1 \rangle$. These features are qualitatively reproduced by the random KHA model of YCOB (Fig. 4c). It is challenging to precisely simulate $1/T_1$, possibly due to the neglecting of the \mathbf{q} dependence of A_{hf} [55]. At $T = 15 \text{ K} \sim 0.3\langle J_1 \rangle$, a weak anomaly (kink) of $1/T_1$ is observed, coinciding with the saturation of local nearest-neighbor correlations $\langle \mathbf{S}_i \cdot \mathbf{S}_j \rangle$ (see Fig. 3d). This is possibly attributed to the emergence of short-range spin correlations, as seen in κ -(ET)₂Cu₂(CN)₃, PbCuTe₂O₆, etc. [50, 59–61].

Discussion

As T further decreases below $\sim 10 \text{ K} \sim 0.2\langle J_1 \rangle$, $1/T_1$ exhibits a weak enhancement, $1/T_1 \sim T^{-\alpha}$ with $\alpha \sim 0.20 \pm 0.02$, at least down to $1.7 \text{ K} \sim 0.03\langle J_1 \rangle$. This weak enhancement of $1/T_1$ is well reproducible between different single-crystal samples, nuclear spin probes (⁸¹Br and ⁷⁹Br), and applied magnetic fields ($\mu_0 H_{\parallel} = 10.75$ and 11.59 T), as shown in Fig. 4. It is necessary to mention that the similar slowing down of spin fluctuations was also reported in other quantum disordered spin systems [62, 63]. Such a behavior of $1/T_1$ suggests the spin system of YCOB may be proximate to a gapless/critical QSL state or highly dynamic valence bond glass with long-range fluctuating singlets:

First, such a temperature dependence of $1/T_1$ is inconsistent with conventional glassy spin freezing. Glassy freezing is typically observed by NMR as a broad peak in $1/T_1$ vs T when the inverse correlation time matches the NMR frequency, and such a peak (T_1 minimum) defines the freezing temperature T_c [64–66]. Moreover, $1/T_1$ is usually expected to increase by more than one order of magnitude at T_c from that above T_c [64–66]. However, such a robust peak in $1/T_1$ vs T is absent in YCOB, as shown in Fig. 4c. Other NMR quantities, line width and $1/T_2$ (Supplementary Fig. 6), also exhibit the common features of well-reported QSL candidates [15, 20, 50, 60, 67, 68], and speak against the existence of well-defined T_c in YCOB (Supplementary Note 5). Note that other experiments, including magnetic and thermodynamic measurements [44–46], also have precluded the possibility of conventional magnetic transition. Thereby, the formation of short-range spin correlations (i.e., $\langle \mathbf{S}_i \cdot \mathbf{S}_j \rangle < 0$) should be responsible for the broadening of NMR lines and enhancement of $1/T_1$ and $1/T_2$ observed at low temperatures in YCOB.

Second, classical spin fluctuations are driven by thermal energy $k_B T$, and cease at low temperatures, $T \ll \langle J_1 \rangle$ [1]. A real example can be the $S = 5/2$ KHA Li₉Fe₃(P₂O₇)₃(PO₄)₂, where the slowing down of classical spin fluctuations, $1/T_1 \sim T^{-1}$, observed just above the antiferromagnetic transition temperature [58], increases much faster than that seen in YCOB, upon cooling. Therefore, the observation of $1/T_1 \sim T^{-0.20 \pm 0.02}$ suggests that quantum fluctuations must play an

important role at low temperatures ($T \leq 0.1\langle J_1 \rangle$) in YCOB.

Third, below $T \sim 0.1\langle J_1 \rangle$, the calculated local nearest-neighbor correlations (Fig. 3d) for the spin system of YCOB level off, manifesting that the observed quantum critical slowing down of spin fluctuations (i.e., $1/T_1 \sim (T - T_c)^{-0.20 \pm 0.02}$ with $T_c \sim 0 \text{ K}$) are associated with a gapless nature of the spin excitations. This is further supported by the nearly quadratic T dependence of specific heat ($C \sim T^{2.31}$) [44]. In contrast, an exponential T -dependent decrease of $1/T_1$ and C with a spin gap of $\geq J_{1c} \sim 16 \text{ K}$ would be expected upon cooling, if the simple product GS of fully quenched random nearest-neighbor singlets is established at low T .

Finally, the system energy gets nearly T -independent (Fig. 4c) and the measured residual spin entropy is small $\sim 3.4\% R \ln 2$ [44], indicating approaching to the disordered GS properties of YCOB at $\sim 1.7 \text{ K}$. We notice that although the temperature decreases by more than two orders of magnitude from 300 to 1.7 K, $1/T_1$ only slightly increases from ~ 380 to 500 s^{-1} , thus suggesting the survival of $\sim 70\%$ of total spin fluctuations at low temperatures (i.e. quantum fluctuations) [24, 54, 63, 67]. Since $1/T_1$ only weakly depends on temperature in the full temperature range between 1.7 and 300 K, $1/(T_1 T) \propto \sum_{\mathbf{q}} \chi''(\mathbf{q}, f_0)$ (see equation (3)) follows a Curie behavior diverging towards $T = 0 \text{ K}$, as shown in Fig. 4d. We also fit the data with the critical function, $1/(T_1 T) \sim (T - T_c)^{-\alpha' - 1}$, in the full temperature range, and find $T_c = -0.1 \pm 0.4 \text{ K} \sim 0 \text{ K}$ and $\alpha' = 0.11(5)$ (see the green lines in Fig. 4d). The dynamical susceptibility ($\sum_{\mathbf{q}} \chi''(\mathbf{q}, f_0)$) relates to the second derivative of the free energy, and thus the observation of $T_c \sim 0 \text{ K}$ (Fig. 4d) indicates a quantum critical behavior. In the paramagnetic limit ($T \rightarrow \infty$), the spin fluctuations including the extremely strong thermal fluctuations ($\propto T$, see ref. [1]) take huge values for an arbitrary spin system. In YCOB, nearly the same Curie behavior, $1/(T_1 T) \propto \sum_{\mathbf{q}} \chi''(\mathbf{q}, f_0) \propto 1/T$, persists from $300 \text{ K} \gg \langle J_1 \rangle$ down to $1.7 \text{ K} \sim 0.03\langle J_1 \rangle$ (see Fig. 4d), thus supporting the survival of strong spin fluctuations toward zero temperature (i.e. quantum fluctuations). All together, these features are in line with the spin dynamics of the putative gapless/critical QSL or dynamic valence bond glass with long-range fluctuating singlets.

We have investigated the local spin susceptibility and dynamics by Br NMR measurements on the high-quality single crystals of YCOB whose randomness has been quantified. The quenched exchange randomness gives rise to the spatially inhomogeneous susceptibility, which accounts for the different T dependencies of Br1 and Br2 main line shifts, as well as broadening. Despite a small fraction of frozen random singlets, the majority of spins of YCOB evade conventional magnetic ordering and remain highly fluctuating, as evidenced by the weak power-law T dependence of $1/T_1$ down to $T \sim 0.03\langle J_1 \rangle$. Our work highlights the role of quantum fluctuations to the gapless QSL behaviors generally observed in relevant materials with inevitable randomness.

Methods

NMR measurements. Two single-crystal samples of YCOB

(S_1 and S_2 with ~ 6.2 and 15.2 mg, respectively) used in NMR measurements were grown by a recrystallization in a temperature gradient [44]. The ^{81}Br ($^{81}\gamma_n = 11.4989$ MHz/T) and ^{79}Br ($^{79}\gamma_n = 10.6675$ MHz/T) NMR measurements were performed using standard spin echo sequences at external magnetic fields ~ 10.75 and 11.59 T aligned to the c axis, between 300 and 1.7 K (the base temperature of our setup). Main NMR shifts of both Br1 and Br2 are derived from the central transitions recorded by a stepped frequency sweep ranging 121 - 125 MHz wherein no satellite transitions from Br can be observed due to the large nuclear quadrupole frequency $\nu_Q > 20$ MHz (Supplementary Note 2 and Supplementary Fig. 3). However, the element of the electric field gradient (EFG) tensor V_{zz} is nearly parallel to the external field, and thus the second-order quadrupole shift is negligibly small (Supplementary Note 6 and Supplementary Figs 7 and 8). Spin-lattice ($1/T_1$) and spin-spin ($1/T_2$) relaxation rates are investigated on Br1 site, measured in inversion recovery and Hahn spin-echo decay methods, respectively (Supplementary Note 3 and Supplementary Fig. 4). The error bars on T_1 come from the standard nonlinear curve fits by using the Origin program, as shown in Fig. 4.

Simulations. We conducted the finite-temperature Lanczos diagonalization simulations of the random KHA model [44] for the NMR line shifts and broadening, local magnetization and correlation, as well as $1/T_1$. No significant finite-size effect of the calculation was observed down to $T \sim 0.1\langle J_1 \rangle$ [44]. The formation energy (see Fig. 1) is calculated as $E(\text{YCu}_3(\text{OH})_{6+x}\text{Br}_{3-x}) - \mu(\text{Y}) - 3\mu(\text{Cu}) - (6+x)\mu(\text{OH}) - (3-x)\mu(\text{Br})$, where the total energy is obtained from the previous density functional theory calculation [44], and $\mu(\text{Y})$, $\mu(\text{Cu})$, $\mu(\text{OH})$, $\mu(\text{Br})$ are the chemical potentials of the constituents. The international system of units is used throughout this paper, and $\langle \rangle$ presents thermal and sample average.

Data availability.

The data sets generated during and/or analysed during the current study are available from the corresponding author on reasonable request.

References

* These authors contributed equally

† mpzsllyk@hust.edu.cn

‡ yuesheng_li@hust.edu.cn

- [1] L. Balents, "Spin liquids in frustrated magnets," *Nature* **464**, 199–208 (2010).
- [2] C. Broholm, R. J. Cava, S. A. Kivelson, D. G. Nocera, M. R. Norman, and T. Senthil, "Quantum spin liquids," *Science* **367**, eaay0668 (2020).
- [3] Y. Kasahara, T. Ohnishi, Y. Mizukami, O. Tanaka, S. Ma, K. Sugii, N. Kurita, H. Tanaka, J. Nasu, Y. Motome, T. Shibauchi, and Y. Matsuda, "Majorana quantization and half-integer thermal quantum Hall effect in a Kitaev spin liquid," *Nature* **559**, 227–231 (2018).
- [4] Y. Zhou, K. Kanoda, and T.-K. Ng, "Quantum spin liquid states," *Rev. Mod. Phys.* **89**, 025003 (2017).
- [5] P. W. Anderson, "Resonating valence bonds: A new kind of insulator?" *Mater. Res. Bull.* **8**, 153–160 (1973).
- [6] P. W. Anderson, "The resonating valence bond state in La_2CuO_4 and superconductivity," *Science* **235**, 1196–1198 (1987).
- [7] C. Nayak, S. H. Simon, A. Stern, M. Freedman, and S. Das Sarma, "Non-Abelian anyons and topological quantum computation," *Rev. Mod. Phys.* **80**, 1083 (2008).
- [8] M. P. Shores, E. A. Nytko, B. M. Bartlett, and D. G. Nocera, "A structurally perfect $S = 1/2$ kagomé antiferromagnet," *J. Am. Chem. Soc.* **127**, 13462–13463 (2005).
- [9] J. S. Helton, K. Matan, M. P. Shores, E. A. Nytko, B. M. Bartlett, Y. Yoshida, Y. Takano, A. Suslov, Y. Qiu, J.-H. Chung, D. G. Nocera, and Y. S. Lee, "Spin dynamics of the spin-1/2 kagome lattice antiferromagnet $\text{ZnCu}_3(\text{OH})_6\text{Cl}_2$," *Phys. Rev. Lett.* **98**, 107204 (2007).
- [10] F. Bert, S. Nakamae, F. Ladieu, D. L'Hôte, P. Bonville, F. Duc, J.-C. Trombe, and P. Mendels, "Low temperature magnetization of the $S = \frac{1}{2}$ kagome antiferromagnet $\text{ZnCu}_3(\text{OH})_6\text{Cl}_2$," *Phys. Rev. B* **76**, 132411 (2007).
- [11] M. A. de Vries, K. V. Kamenev, W. A. Kockelmann, J. Sanchez-Benitez, and A. Harrison, "Magnetic ground state of an experimental $S = 1/2$ kagome antiferromagnet," *Phys. Rev. Lett.* **100**, 157205 (2008).
- [12] T.-H. Han, J. S. Helton, S. Chu, D. G. Nocera, J. A. Rodriguez-Rivera, C. Broholm, and Y. S. Lee, "Fractionalized excitations in the spin-liquid state of a kagome-lattice antiferromagnet," *Nature* **492**, 406 (2012).
- [13] T.-H. Han, M. R. Norman, J.-J. Wen, J. A. Rodriguez-Rivera, J. S. Helton, C. Broholm, and Y. S. Lee, "Correlated impurities and intrinsic spin-liquid physics in the kagome material herbertsmithite," *Phys. Rev. B* **94**, 060409 (2016).
- [14] A. Olariu, P. Mendels, F. Bert, F. Duc, J. C. Trombe, M. A. de Vries, and A. Harrison, " ^{17}O NMR study of the intrinsic magnetic susceptibility and spin dynamics of the quantum kagome antiferromagnet $\text{ZnCu}_3(\text{OH})_6\text{Cl}_2$," *Phys. Rev. Lett.* **100**, 087202 (2008).
- [15] M. Fu, T. Imai, T.-H. Han, and Y. S. Lee, "Evidence for a gapped spin-liquid ground state in a kagome Heisenberg antiferromagnet," *Science* **350**, 655–658 (2015).
- [16] P. Khuntia, M. Velazquez, Q. Barthélemy, F. Bert, E. Kermarrec, A. Legros, B. Bernu, L. Messio, A. Zorko, and P. Mendels, "Gapless ground state in the archetypal quantum kagome antiferromagnet $\text{ZnCu}_3(\text{OH})_6\text{Cl}_2$," *Nat. Phys.* **16**, 469–474 (2020).
- [17] M. R. Norman, "Colloquium: Herbertsmithite and the search for the quantum spin liquid," *Rev. Mod. Phys.* **88**, 041002 (2016).
- [18] Y. Shimizu, K. Miyagawa, K. Kanoda, M. Maesato, and G. Saito, "Spin liquid state in an organic Mott insulator with a triangular lattice," *Phys. Rev. Lett.* **91**, 107001 (2003).
- [19] S. Yamashita, Y. Nakazawa, M. Oguni, Y. Oshima, H. Nojiri, Y. Shimizu, K. Miyagawa, and K. Kanoda, "Thermodynamic properties of a spin-1/2 spin-liquid state in a κ -type organic salt," *Nat. Phys.* **4**, 459 (2008).
- [20] T. Itou, A. Oyamada, S. Maegawa, M. Tamura, and R. Kato, "Quantum spin liquid in the spin-1/2 triangular antiferromagnet $\text{EtMe}_3\text{Sb}[\text{Pd}(\text{dmit})_2]_2$," *Phys. Rev. B* **77**, 104413 (2008).
- [21] T. Itou, A. Oyamada, S. Maegawa, and R. Kato, "Instability of a quantum spin liquid in an organic triangular-lattice antiferro-

- magnet,” *Nat. Phys.* **6**, 673 (2010).
- [22] Y. Li, H. Liao, Z. Zhang, S. Li, F. Jin, L. Ling, L. Zhang, Y. Zou, L. Pi, Z. Yang, J. Wang, Z. Wu, and Q. Zhang, “Gapless quantum spin liquid ground state in the two-dimensional spin-1/2 triangular antiferromagnet YbMgGaO_4 ,” *Sci. Rep.* **5**, 16419 (2015).
- [23] Y. Li, G. Chen, W. Tong, L. Pi, J. Liu, Z. Yang, X. Wang, and Q. Zhang, “Rare-earth triangular lattice spin liquid: A single-crystal study of YbMgGaO_4 ,” *Phys. Rev. Lett.* **115**, 167203 (2015).
- [24] Y. Li, D. Adroja, P. K. Biswas, P. J. Baker, Q. Zhang, J. Liu, A. A. Tsirlin, P. Gegenwart, and Q. Zhang, “Muon spin relaxation evidence for the $U(1)$ quantum spin-liquid ground state in the triangular antiferromagnet YbMgGaO_4 ,” *Phys. Rev. Lett.* **117**, 097201 (2016).
- [25] Y. Shen, Y. Li, H. Wo, Y. Li, S. Shen, B. Pan, Q. Wang, H. C. Walker, P. Steffens, M. Boehm, Y. Hao, D. L. Quintero-Castro, L. W. Harriger, M. D. Frontzek, L. Hao, S. Meng, Q. Zhang, G. Chen, and J. Zhao, “Evidence for a spinon Fermi surface in a triangular-lattice quantum-spin-liquid candidate,” *Nature* **540**, 559–562 (2016).
- [26] J. A. M. Paddison, M. Daum, Z. Dun, G. Ehlers, Y. Liu, M. B. Stone, H. Zhou, and M. Mourigal, “Continuous excitations of the triangular-lattice quantum spin liquid YbMgGaO_4 ,” *Nature Phys.* **13**, 117–122 (2017).
- [27] Y. Li, S. Bachus, B. Liu, I. Radelytskyi, A. Bertin, A. Schneidewind, Y. Tokiwa, A. A. Tsirlin, and P. Gegenwart, “Rearrangement of uncorrelated valence bonds evidenced by low-energy spin excitations in YbMgGaO_4 ,” *Phys. Rev. Lett.* **122**, 137201 (2019).
- [28] Y. Y. Huang, Y. Xu, Le Wang, C. C. Zhao, C. P. Tu, J. M. Ni, L. S. Wang, B. L. Pan, Ying Fu, Zhanyang Hao, Cai Liu, Jia-Wei Mei, and S. Y. Li, “Heat transport in Herbertsmithite: Can a quantum spin liquid survive disorder?” *Phys. Rev. Lett.* **127**, 267202 (2021).
- [29] H. Murayama, T. Tominaga, T. Asaba, A. de Oliveira Silva, Y. Sato, H. Suzuki, Y. Ukai, S. Suetsugu, Y. Kasahara, R. Okuma, I. Kimchi, and Y. Matsuda, “Universal scaling of the specific heat in $S = \frac{1}{2}$ quantum kagome antiferromagnet herbertsmithite,” *arXiv preprint arXiv:2106.07223* (2021).
- [30] J. M. Ni, B. L. Pan, B. Q. Song, Y. Y. Huang, J. Y. Zeng, Y. J. Yu, E. J. Cheng, L. S. Wang, D. Z. Dai, R. Kato, and S. Y. Li, “Absence of magnetic thermal conductivity in the quantum spin liquid candidate $\text{EtMe}_3\text{Sb}[\text{Pd}(\text{dmit})_2]_2$,” *Phys. Rev. Lett.* **123**, 247204 (2019).
- [31] P. Bourgeois-Hope, F. Laliberté, E. Lefrançois, G. Grissonnanche, S. René de Cotret, R. Gordon, S. Kitou, H. Sawa, H. Cui, R. Kato, L. Taillefer, and N. Doiron-Leyraud, “Thermal conductivity of the quantum spin liquid candidate $\text{EtMe}_3\text{Sb}[\text{Pd}(\text{dmit})_2]_2$: No evidence of mobile gapless excitations,” *Phys. Rev. X* **9**, 041051 (2019).
- [32] Y. Xu, J. Zhang, Y. S. Li, Y. J. Yu, X. C. Hong, Q. M. Zhang, and S. Y. Li, “Absence of magnetic thermal conductivity in the quantum spin-liquid candidate YbMgGaO_4 ,” *Phys. Rev. Lett.* **117**, 267202 (2016).
- [33] T. Shimokawa, K. Watanabe, and H. Kawamura, “Static and dynamical spin correlations of the $S = \frac{1}{2}$ random-bond antiferromagnetic Heisenberg model on the triangular and kagome lattices,” *Phys. Rev. B* **92**, 134407 (2015).
- [34] H. J. Liao, Z. Y. Xie, J. Chen, Z. Y. Liu, H. D. Xie, R. Z. Huang, B. Normand, and T. Xiang, “Gapless spin-liquid ground state in the $S = 1/2$ kagome antiferromagnet,” *Phys. Rev. Lett.* **118**, 137202 (2017).
- [35] C.-Y. Lee, B. Normand, and Y.-J. Kao, “Gapless spin liquid in the kagome Heisenberg antiferromagnet with Dzyaloshinskii-Moriya interactions,” *Phys. Rev. B* **98**, 224414 (2018).
- [36] P. A. Lee, N. Nagaosa, and X.-G. Wen, “Doping a Mott insulator: Physics of high-temperature superconductivity,” *Rev. Mod. Phys.* **78**, 17–85 (2006).
- [37] R. R. P. Singh, “Valence bond glass phase in dilute kagome antiferromagnets,” *Phys. Rev. Lett.* **104**, 177203 (2010).
- [38] H. Kawamura, K. Watanabe, and T. Shimokawa, “Quantum spin-liquid behavior in the spin-1/2 random-bond Heisenberg antiferromagnet on the kagome lattice,” *J. Phys. Soc. Jpn.* **83**, 103704 (2014).
- [39] H. Watanabe, K. Kawamura, T. Shimokawa, and T. Sakai, “Quantum spin-liquid behavior in the spin-1/2 random Heisenberg antiferromagnet on the triangular lattice,” *J. Phys. Soc. Jpn.* **83**, 034714 (2014).
- [40] Z. Zhu, P. A. Maksimov, S. R. White, and A. L. Chernyshev, “Disorder-induced mimicry of a spin liquid in YbMgGaO_4 ,” *Phys. Rev. Lett.* **119**, 157201 (2017).
- [41] I. Kimchi, A. Nahum, and T. Senthil, “Valence bonds in random quantum magnets: Theory and application to YbMgGaO_4 ,” *Phys. Rev. X* **8**, 031028 (2018).
- [42] Y. Li, D. Adroja, R. I. Bewley, D. Voneshen, A. A. Tsirlin, P. Gegenwart, and Q. Zhang, “Crystalline electric-field randomness in the triangular lattice spin-liquid YbMgGaO_4 ,” *Phys. Rev. Lett.* **118**, 107202 (2017).
- [43] I. Kimchi, J. P. Sheckelton, T. M. McQueen, and P. A. Lee, “Scaling and data collapse from local moments in frustrated disordered quantum spin systems,” *Nat. Commun.* **9**, 4367 (2018).
- [44] J. Liu, L. Yuan, X. Li, B. Li, K. Zhao, H. Liao, and Y. Li, “Gapless spin liquid behavior in a kagome Heisenberg antiferromagnet with randomly distributed hexagons of alternate bonds,” *Phys. Rev. B* **105**, 024418 (2022).
- [45] X.-H. Chen, Y.-X. Huang, Y. Pan, and J.-X. Mi, “Quantum spin liquid candidate $\text{YCu}_3(\text{OH})_6\text{Br}_2[\text{Br}_x(\text{OH})_{1-x}]$ ($x \approx 0.51$): With an almost perfect kagomé layer,” *J. Magn. Mater.* **512**, 167066 (2020).
- [46] Z. Zeng, X. Ma, S. Wu, H.-F. Li, Z. Tao, X. Lu, X.-h. Chen, J.-X. Mi, S.-J. Song, G.-H. Cao, G. Che, K. Li, G. Li, H. Luo, Z. Y. Meng, and S. Li, “Possible Dirac quantum spin liquid in the kagome quantum antiferromagnet $\text{YCu}_3(\text{OH})_6\text{Br}_2[\text{Br}_x(\text{OH})_{1-x}]$,” *Phys. Rev. B* **105**, L121109 (2022).
- [47] X. Hong, M. Behnami, L. Yuan, B. Li, W. Brenig, B. Büchner, Y. Li, and C. Hess, “Heat transport of the kagomé Heisenberg quantum spin liquid candidate $\text{YCu}_3(\text{OH})_{6.5}\text{Br}_{2.5}$: localized magnetic excitations and spin gap,” *arXiv preprint arXiv:2205.13667* (2022).
- [48] T. Imai, E. A. Nytko, B. M. Bartlett, M. P. Shores, and D. G. Nocera, “ ^{63}Cu , ^{35}Cl , and ^1H NMR in the $s = \frac{1}{2}$ kagome lattice $\text{ZnCu}_3(\text{OH})_6\text{Cl}_2$,” *Phys. Rev. Lett.* **100**, 077203 (2008).
- [49] T. Imai, M. Fu, T. H. Han, and Y. S. Lee, “Local spin susceptibility of the $s = \frac{1}{2}$ kagome lattice in $\text{ZnCu}_3(\text{OH})_6\text{Cl}_2$,” *Phys. Rev. B* **84**, 020411 (2011).
- [50] P. Khuntia, F. Bert, P. Mendels, B. Koteswararao, A. V. Mahajan, M. Baenitz, F. C. Chou, C. Baines, A. Amato, and Y. Furukawa, “Spin liquid state in the 3D frustrated antiferromagnet $\text{PbCuTe}_2\text{O}_6$: NMR and muon spin relaxation studies,” *Phys. Rev. Lett.* **116**, 107203 (2016).
- [51] Y. Li, “ YbMgGaO_4 : A triangular-lattice quantum spin liquid candidate,” *Adv. Quantum Technol.* **2**, 1900089 (2019).
- [52] Y. Li, P. Gegenwart, and A. A. Tsirlin, “Spin liquids in geometrically perfect triangular antiferromagnets,” *J. Phys.: Condens. Matter* **32**, 224004 (2020).
- [53] <https://www.originlab.com/doc/>

Origin-Help/Interpret-Regression-Result.

- [54] S. Kitagawa, K. Ishida, T. Nakamura, M. Matoba, and Y. Kamihara, “Ferromagnetic quantum critical point in heavy-fermion iron oxypnictide $\text{Ce}(\text{Ru}_{1-x}\text{Fe}_x)\text{PO}_4$,” *Phys. Rev. Lett.* **109**, 227004 (2012).
- [55] P. Prelovšek, M. Gomilšek, T. Arh, and A. Zorko, “Dynamical spin correlations of the kagome antiferromagnet,” *Phys. Rev. B* **103**, 014431 (2021).
- [56] Y. Li, S. Bachus, H. Deng, W. Schmidt, H. Thoma, V. Hutanu, Y. Tokiwa, A. A. Tsirlin, and P. Gegenwart, “Partial up-down order with the continuously distributed order parameter in the triangular antiferromagnet TmMgGaO_4 ,” *Phys. Rev. X* **10**, 011007 (2020).
- [57] S. Moriya, “Nuclear magnetic relaxation in antiferromagnets,” *Prog. Theor. Phys.* **16**, 23 (1956).
- [58] E. Kermarrec, R. Kumar, G. Bernard, R. Hénaff, P. Mendels, F. Bert, P. L. Paulose, B. K. Hazra, and B. Koteswararao, “Classical spin liquid state in the $S = \frac{5}{2}$ Heisenberg kagome antiferromagnet $\text{Li}_9\text{Fe}_3(\text{P}_2\text{O}_7)_3(\text{PO}_4)_2$,” *Phys. Rev. Lett.* **127**, 157202 (2021).
- [59] T. Furukawa, K. Miyagawa, T. Itou, M. Ito, H. Taniguchi, M. Saito, S. Iguchi, T. Sasaki, and K. Kanoda, “Quantum spin liquid emerging from antiferromagnetic order by introducing disorder,” *Phys. Rev. Lett.* **115**, 077001 (2015).
- [60] Y. Shimizu, K. Miyagawa, K. Kanoda, M. Maesato, and G. Saito, “Emergence of inhomogeneous moments from spin liquid in the triangular-lattice Mott insulator κ -(ET) $_2\text{Cu}_2(\text{CN})_3$,” *Phys. Rev. B* **73**, 140407 (2006).
- [61] J. Wang, W. Yuan, T. Imai, P. M. Singer, F. Bahrami, and F. Tafti, “NMR investigation on the honeycomb iridate $\text{Ag}_3\text{LiIr}_2\text{O}_6$,” *Phys. Rev. B* **103**, 214405 (2021).
- [62] A. W. Kinross, M. Fu, T. J. Munsie, H. A. Dabkowska, G. M. Luke, S. Sachdev, and T. Imai, “Evolution of quantum fluctuations near the quantum critical point of the transverse field Ising chain system CoNb_2O_6 ,” *Phys. Rev. X* **4**, 031008 (2014).
- [63] S. Lee, S.-H. Do, W. Lee, Y. S. Choi, J. van Tol, A. P. Reyes, D. Gorbunov, W.-T. Chen, and K.-Y. Choi, “Dichotomy in temporal and thermal spin correlations observed in the breathing pyrochlore $\text{LiGa}_{1-x}\text{In}_x\text{Cr}_4\text{O}_8$,” *npj Quantum Materials* **6**, 1–8 (2021).
- [64] M.-H. Julien, F. Borsa, P. Carretta, M. Horvatić, C. Berthier, and C. T. Lin, “Charge segregation, cluster spin glass, and superconductivity in $\text{La}_{1.94}\text{Sr}_{0.06}\text{CuO}_4$,” *Phys. Rev. Lett.* **83**, 604–607 (1999).
- [65] X. Zong, A. Niazi, F. Borsa, X. Ma, and D. C. Johnston, “Structure, magnetization, and NMR studies of the spin-glass compound $(\text{Li}_x\text{V}_{1-x})_3\text{BO}_5$ ($x \approx 0.40$ and 0.33),” *Phys. Rev. B* **76**, 054452 (2007).
- [66] M. Frachet, I. Vinograd, R. Zhou, S. Benhabib, S. Wu, H. Mayaffre, S. Krämer, S. K. Ramakrishna, A. P. Reyes, J. Debray, T. Kurosawa, N. Momono, M. Oda, S. Komiyama, S. Ono, M. Horio, J. Chang, C. Proust, D. LeBoeuf, and M.-H. Julien, “Hidden magnetism at the pseudogap critical point of a cuprate superconductor,” *Nat. Phys.* **16**, 1064 (2020).
- [67] S. Lee, C. H. Lee, A. Berlie, A. D. Hillier, D. T. Adroja, R. Zhong, R. J. Cava, Z. H. Jang, and K.-Y. Choi, “Temporal and field evolution of spin excitations in the disorder-free triangular antiferromagnet $\text{Na}_2\text{BaCo}(\text{PO}_4)_2$,” *Phys. Rev. B* **103**, 024413 (2021).
- [68] J. A. Quilliam, F. Bert, A. Manseau, C. Darie, C. Guillot-Deudon, C. Payen, C. Baines, A. Amato, and P. Mendels, “Gapless quantum spin liquid ground state in the spin-1 antiferromagnet $6\text{HB-Ba}_3\text{NiSb}_2\text{O}_9$,” *Phys. Rev. B* **93**, 214432 (2016).

Acknowledgements

We thank Philipp Gegenwart, Alexander A. Tsirlin, Christian Hess, Xiaochen Hong, and Haijun Liao for insightful discussions, and Long Ma for technical helps. This work was supported by the Fundamental Research Funds for the Central Universities (HUST: 2020kfyXJJS054) and the open research fund of Songshan Lake Materials Laboratory (2022SLABFN27).

Author contributions

Y.K.L. and Y.S.L. planned the experiments. L.Y., B.Q.L. and Y.S.L. synthesized and characterized the sample. F.J.L., J.Z. and Y.K.L. collected the NMR data. F.J.L., Y.K.L. and Y.S.L. analysed the data. Y.S.L. conducted the quantum many-body and first-principles computations. Y.S.L. and Y.K.L. wrote the manuscript with comments from all co-authors. The manuscript reflects the contributions of all authors.

Competing interests

The authors declare no competing interests.

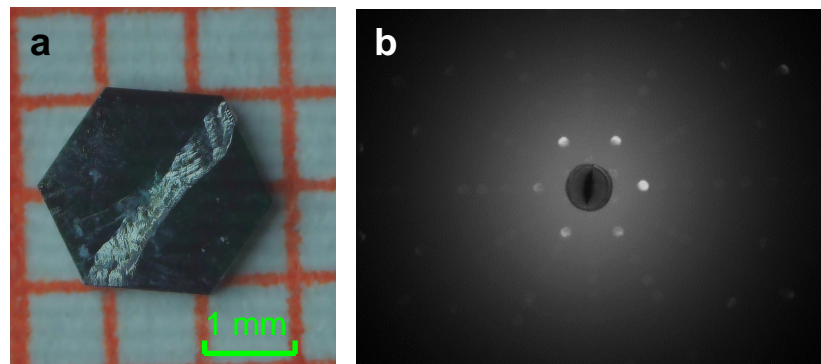
Supplementary Information

The observation of quantum fluctuations in a kagome Heisenberg antiferromagnet

Fangjun Lu, Long Yuan, Jian Zhang, Boqiang Li, Yongkang Luo, and Yuesheng Li

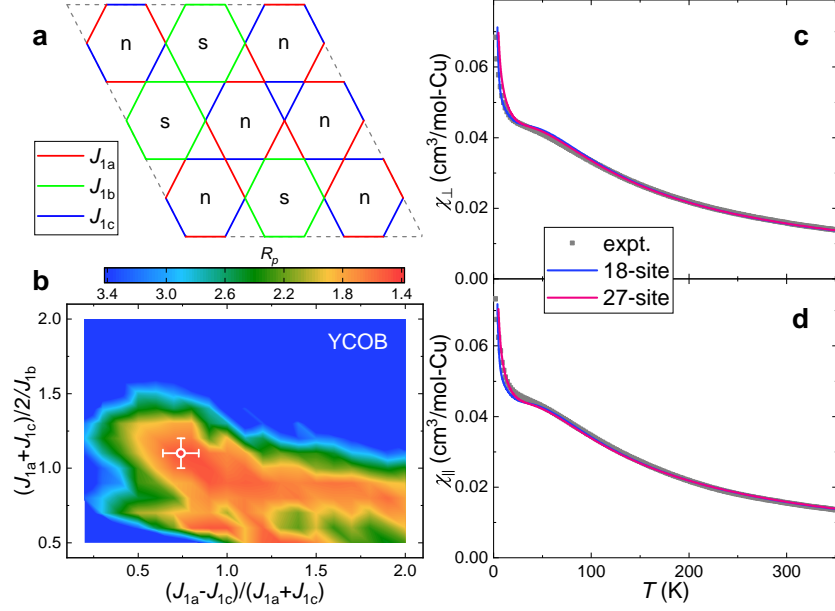
Supplementary Note 1. Refinement of the random exchange Hamiltonian

The previously reported crystal structure determined by single-crystal XRD and density functional theory (DFT) calculation with a Coulomb repulsion (U) has revealed that the inherent antisite disorder of polar OH_2^- and nonpolar Br_2^- pushes 70(2)% of Y^{3+} away from its ideal position by a distance of $\Delta z_{\text{Y}2} \sim \pm 0.7\text{\AA}$ and this influences the nearest-neighbor (NN) exchange couplings (J_1) of the kagome Heisenberg antiferromagnet (KHA) YCOB [1]. The nonsymmetric local environments of $\text{OH}_2^-/\text{Br}_2^-$ give rise to hexagons with alternate exchanges (J_{1a} and J_{1c}) on the kagome lattice, whereas the rest symmetric stacking sequences of $\text{OH}_2^-/\text{Br}_2^-$ result in almost uniform hexagons (J_{1b}), as illustrated in Supplementary Fig. 2a. The DFT+ U calculations suggest that both further-neighbor and interlayer exchange couplings are less than 4% of $\langle J_1 \rangle$ [1], due to the spatial localization of the 3d electrons in the insulating YCOB. The measured magnetic anisotropy, $\chi_{\parallel}/\chi_{\perp}$, only increases by $\sim 4\%$ from $T = \langle J_1 \rangle$ down to 1.8 K $\sim 0.03\langle J_1 \rangle$ [1], suggesting that the interaction anisotropy is not critical due to the weak spin-orbit coupling of the 3d electrons.



Supplementary Figure 1. Single crystal used in NMR measurements. (a) The single crystal (S_1) of $\text{YCu}_3(\text{OH})_{6.5}\text{Br}_{2.5}$ (YCOB) used in NMR measurements. (b) Laue x-ray diffraction (XRD) pattern measured on the ab plane, i.e., the largest surface of the single crystal shown in a.

Analogous to the simplified crystal structure of YCOB [2] with three discrete Y positions, $\Delta z_{\text{Y}1} = 0$ and $\Delta z_{\text{Y}2} \sim \pm 0.7\text{\AA}$, we constructed a similarly simplified random exchange model with three discrete couplings, J_{1a} , J_{1b} , and J_{1c} , on the kagome lattice (Supplementary Fig. 2a). The real situation might be much more complicated, but we seek to explain the experimental observations within a minimum model that



Supplementary Figure 2. Refinement of the exchange Hamiltonian. (a) Sketch of a random KHA sample with $1 - f_{Y1} \sim 0.7$ of randomly distributed nonsymmetric (n) hexagons of alternate exchanges (blue and red) and the rest of symmetric (s) hexagons (green). (b) The deviation R_p^a obtained by fitting the magnetic susceptibilities with fixed occupancy $f_{Y1} = 0.3$ (experimentally determined by single-crystal XRD). The magnetic susceptibilities of YCOB measured at 1 T are shown in panels c and d, for field applied along the ab plane and c axis, respectively. The colored lines show the FTLD susceptibilities calculated on the 18- and 27-site clusters with periodic boundary conditions, using $J_{1a} = 89.4$ K, $J_{1b} = 47.9$ K, and $J_{1c} = 15.8$ K.

$$^a R_p = \sqrt{\frac{1}{N_0} \sum_i \left(\frac{X_i^{\text{obs}} - X_i^{\text{cal}}}{\sigma_i^{\text{obs}}} \right)^2},$$

where N_0 , X_i^{obs} and σ_i^{obs} are the number of the data points, the observed value and its standard deviation, respectively, whereas X_i^{cal} is the calculated value.

captures the essential physics. The observables calculated by the 18- and 27-site finite-temperature Lanczos diagonalization (FTLD) are evaluated over 80 and 30 independent samples, respectively. For the simulation of the dynamic spin-lattice relaxation rate ($1/T_1$), more than 100 Lanczos steps are typically required. From fitting the magnetic susceptibilities above $6 \text{ K} \sim 0.1 \langle J_1 \rangle$ (see Supplementary Fig. 2c,d), we obtain $J_{1a} = 89$ K, $J_{1b} = 48$ K, and $J_{1c} = 16$ K with the least $R_p = 1.4(1)$. The resulted $(J_{1a} - J_{1c})/(J_{1a} + J_{1c}) = 0.7(1)$, $(J_{1a} + J_{1c})/(2J_{1b}) = 1.1(1)$, and $\langle J_1 \rangle = 0.35J_{1a} + 0.3J_{1b} + 0.35J_{1c} \sim 51$ K are well consistent with the previously reported result [1] (Supplementary Fig. 2b). Furthermore, the resulted $R_p = 1.4(1)$ is very close to the lower limit $R_p \sim 1$, and the finite-size effect of the FTLD calculation is negligible above $T \sim 0.1 \langle J_1 \rangle$ (see Supplementary Fig. 2c,d), proving the validity of this random exchange model.

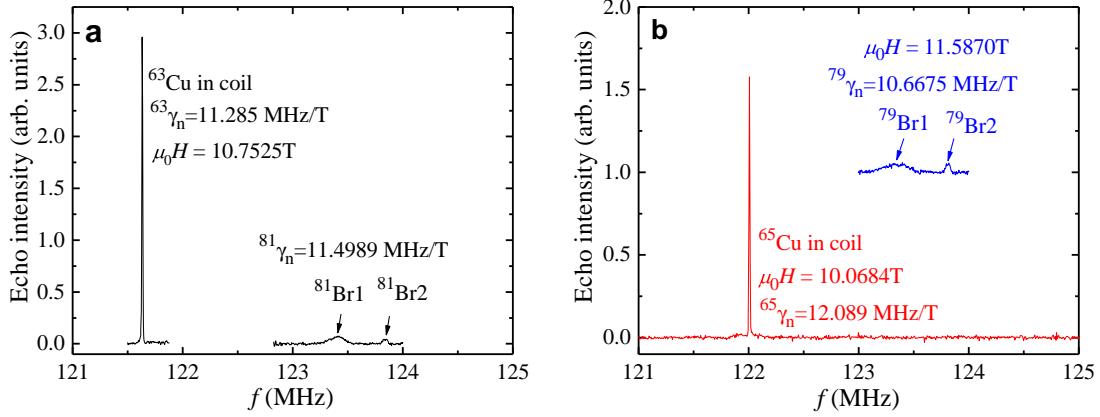
Due to the inherent exchange randomness, different bricks of spins (S_i) on the kagome lattice of YCOB have different local magnetization at a magnetic field and low temperatures, $\langle S^z \rangle = \sum_{i \in \text{brick}} \langle S_i^z \rangle / N_{\text{brick}}$, where $N_{\text{brick}} = 3$ or 6 is the number of spins in each triangular or hexagonal brick, respectively, and $\langle S_i^z \rangle = \sum_m e^{-\frac{E_m}{k_B T}} \langle m | S_i^z | m \rangle / \sum_m e^{-\frac{E_m}{k_B T}}$. In our 27-site FTLD calculation, 30 independent samples are taken into account to simulate the effect of quenched randomness, and thus there are $27 \times 30 = 810$ spins, $810 \times 2/3 = 540$ triangles, $810/3 \times 0.7 = 189$ nonsymmetric hexagons, and $810/3 \times 0.3 = 81$ symmetric hexagons. Therefore, one can define the distributed density function, $dn_S(\langle S^z \rangle)/d\langle S^z \rangle$, which depends on T and accounts for the broadening of the NMR main lines. Here, $dn_S(\langle S^z \rangle)$ is the number of bricks with the local magnetization (per site) ranging from $\langle S^z \rangle$ to $\langle S^z \rangle + d\langle S^z \rangle$.

Supplementary Note 2. Identification of ^{81}Br and ^{79}Br NMR

Because the gyromagnetic ratio of ^{63}Cu ($^{63}\gamma_n = 11.285 \text{ MHz/T}$) and ^{81}Br ($^{81}\gamma_n = 11.4989 \text{ MHz/T}$) are close, the ^{63}Cu signal from the copper coil can be regarded as the hallmark of these measurements. Supplementary Fig. 3a displays a representative spectrum taken at $T = 265 \text{ K}$ and $\mu_0 H_{\parallel} \sim 10.75 \text{ T}$. Three peaks can be seen in the frequency window 121-125 MHz. The sharp peak centered at 121.632 MHz has a full width at half maximum (FWHM) only $\sim 10 \text{ kHz}$, it, therefore, is reasonable to ascribe it as ^{63}Cu in coil. This leads to a precise magnetic field value $\mu_0 H_{\parallel} = 10.7525 \text{ T}$ with the Knight shift of elemental Cu $K = 0.2394\%$ already known [3]. The two other peaks near 123.41 MHz and 123.84 MHz can not originate from ^{63}Cu in YCOB, because they disappear when we attempted to detect them in the ^{65}Cu measurements (cf the red curve in Supplementary Fig. 3b), but instead they show up in the ^{79}Br measurements under $\mu_0 H_{\parallel} = 11.5870 \text{ T}$. The NMR shifts of Br2 and Br1 determined from ^{79}Br and ^{81}Br are in good agreement. Furthermore, the weight ratio between these two peaks is $I_{\text{Br2}}/I_{\text{Br1}} \sim 0.2$, close to the stoichiometric ratio of Br2 and Br1 determined by single-crystal XRD (see inset of Fig. 2b in main text), and this provides additional evidence that the two peaks respectively stem from Br2 and Br1 sites in YCOB. Note that no satellite transitions arising from nuclear quadruple effect related to ^{81}Br (nuclear spin $I = 3/2$) can be resolved in this frequency range. The missing of ^{63}Cu signal from YCOB is probably due to a large NMR shift (thus is moved out from the detected frequency range) or a very short spin-spin relaxation time (T_2 wipe-out), and further measurements are required to clarify this issue.

Supplementary Note 3. Br1 nuclear spin-lattice and spin-spin relaxation

Spin-lattice relaxation rate ($1/T_1$) of Br1 was measured by the inversion recovery method whose pulse sequence is depicted in the inset of Fig. 4a in the main text. The T_1 relaxation data can be fitted to a



Supplementary Figure 3. Frequency sweep spectra (121-125 MHz) taken at 265 K. (a) At $\mu_0 H_{\parallel} = 10.7525$ T, one sees three peaks arising from ^{63}Cu in coil, $^{81}\text{Br1}$ and $^{81}\text{Br2}$ in YCOB sample, respectively. (b) Red curve, at $\mu_0 H_{\parallel} = 10.0684$ T, only one sharp peak is resolved, from ^{65}Cu in coil. Blue curve, at $\mu_0 H_{\parallel} = 11.5870$ T, two relatively broader peaks can be seen which are attributed to ^{79}Br of the sample. The base line of the blue curve has been shifted vertically for clarity.

stretched-exponential function for the central transition of $I = 3/2$ nuclear spins, i.e.,

$$M(t)|_{-\frac{1}{2} \leftrightarrow \frac{1}{2}} = M_0 - 2M_0 F \left\{ \frac{1}{10} \exp\left[-\left(\frac{t}{T_1}\right)^\beta\right] + \frac{9}{10} \exp\left[-\left(\frac{6t}{T_1}\right)^\beta\right] \right\}. \quad (1)$$

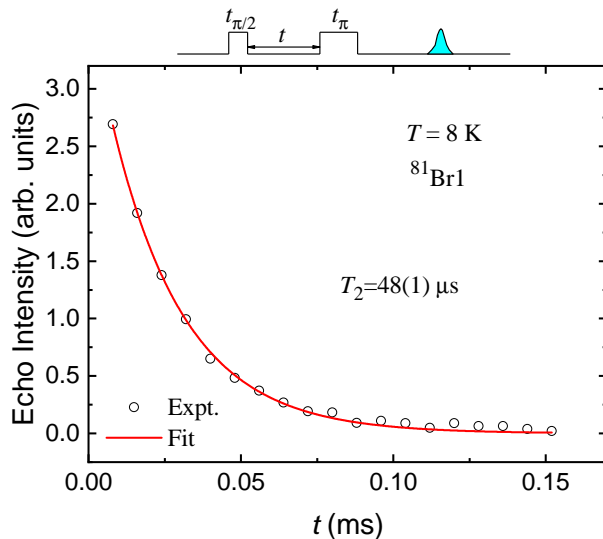
When the stretching exponent is fixed to $\beta = 1$, Supplementary equation (1) gets back to the standard formula. From fitting the data measured at 2.8 K (< 15 K), we find that including the additional fitting parameter β only slightly increases the adj. R^2 [4] from 0.9975 (at $\beta = 1$) to 0.9982 (at $\beta = 0.83$), and the fitted $\beta = 0.83(9)$ is much larger than $\sim 1/3$ expected for a conventional spin-glass freezing [5]. Our experimental observations suggest the T_1 relaxation is not strongly stretched even at low temperatures.

Spin-spin relaxation rate ($1/T_2$) of Br1 was measured by the Hahn spin-echo decay method, the pulse sequence of which is sketched on the top of Supplementary Fig. 4. A representative result of 8 K is shown in Supplementary Fig. 4 as an example. The spin-echo intensity $M(2t)$ decreases with the increasing time interval between the $\pi/2$ and π pulses, following the exponential function:

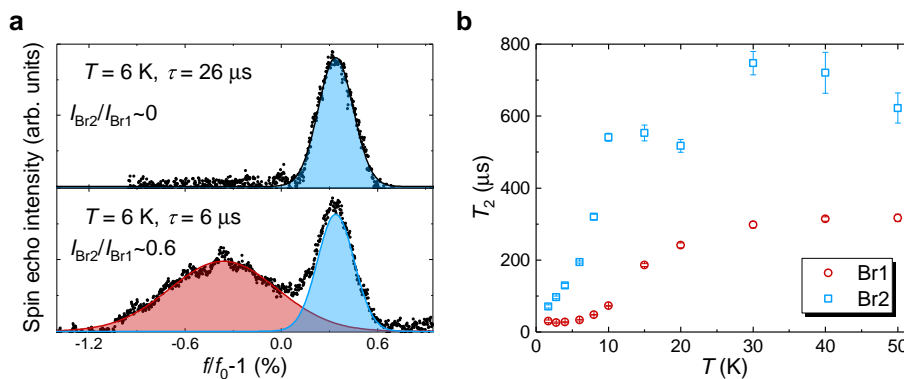
$$M(2t) = M_0 \exp(-2t/T_2). \quad (2)$$

This fitting yields $T_2 = 48(1) \mu\text{s}$ for $T = 8$ K.

Supplementary Note 4. Low- T NMR spectra measured with different delays of the spin-echo sequences



Supplementary Figure 4. Nuclear spin-spin relaxation. A selected $T = 8$ K spin-spin relaxation of Br1 measured by Hahn spin-echo decay method, fitted to Supplementary equation (2). The symbols denote the experimental results, while the red lines are the fitting curves. The pulse sequence for T_2 measurements is depicted on the top of the figure.



Supplementary Figure 5. NMR spectra and transverse relaxation times. (a) Frequency-sweep NMR spectra of YCOB measured with different delays τ of the spin-echo sequences at 6 K. (b) Temperature dependence of transverse relaxation times $T_2(\text{Br1})$ and $T_2(\text{Br2})$.

Supplementary Fig. 5a shows the NMR spectra measured with different delays τ of the spin-echo sequences, at the same low temperature of 6 K (< 15 K). When a typical τ of $26 \mu\text{s}$ is used, the broader NMR line from Br1 nuclear spins disappears at low temperatures, due to the short transverse relaxation time $T_2(\text{Br1})$ of $33(2) \mu\text{s}$ (Supplementary Fig. 5b) that is compatible with τ . In contrast, when using the shortest

delay $\tau = 6 \mu\text{s}$ of our setup the situation gets much better and the Br1 NMR line appears again. However, the ratio between the *integrated* intensities, $I_{\text{Br2}}/I_{\text{Br1}}$, sharply increases to ~ 0.6 below 15 K (please see the inset of Fig. 2b of the main text), and thus the overall intensity of the Br1 NMR line is still significantly suppressed due to the short $T_2(\text{Br1})$, which is still compatible with $\tau = 6 \mu\text{s}$. For the Br2 NMR line the suppression of the intensity is less apparent, because $T_2(\text{Br2})$ is about two times larger than $T_2(\text{Br1})$ in the full temperature range, which is another strong signature of different origins of the Br1 and Br2 NMR lines.

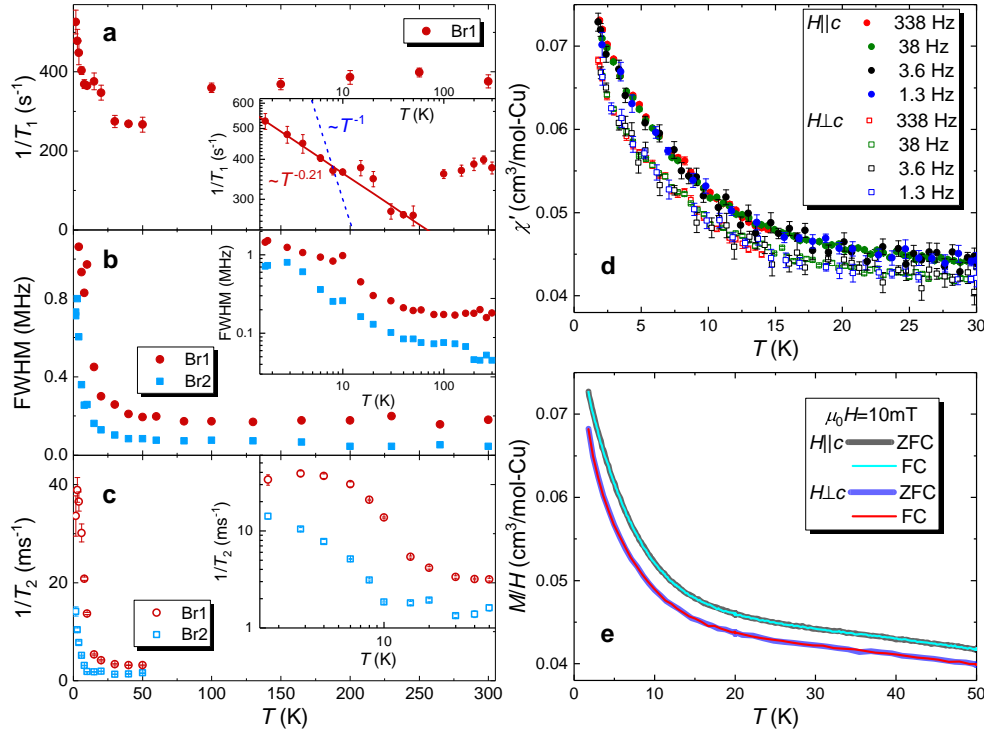
Supplementary Note 5. Absence of conventional spin freezing

Glassy freezing/dynamics is typically observed by NMR as a broad peak in the nuclear spin-lattice relaxation rate $1/T_1$ vs temperature T when the inverse correlation time matches the NMR frequency, and such a peak (T_1 minimum) defines the freezing temperature T_c [6–8]. Moreover, $1/T_1$ is usually expected to increase by more than one order of magnitude at T_c from that above T_c , as reported in refs [6–8] for example. However, such a robust peak in $1/T_1$ vs T is absent in YCOB, as shown in Supplementary Fig. 6a. Therefore, conventional spin-glass freezing between 1.7 and 300 K should be precluded. Furthermore, both ac and dc susceptibilities also do not exhibit any peak features (see Supplementary Fig. 6d,e). Neither obvious frequency dependence of ac susceptibilities nor splitting of ZFC and FC dc susceptibilities was observed [1, 2, 9], confirming the absence of any conventional spin-glass freezing down to 1.8 K in YCOB.

Neither $1/T_1$ nor $1/T_2$ of YCOB shows any conventional critical enhancement (peak) in their temperature dependence (see Supplementary Fig. 6), which speaks against the presence of conventional spin freezing at $T \geq 1.7 \text{ K} \sim 0.03\langle J_1 \rangle$. Moreover, as reported in our previous bulk study the residual magnetic entropy of YCOB obtained from the specific heat gets small below 1.7 K, $S_m \leq 3.4\% R \ln 2$ [1], suggesting the approaching of ground-state properties. These observations consistently suggests that the majority of spins remain disordered at low temperatures.

Of course, the enhancement of the $1/T_1$ and $1/T_2$ at low T indeed indicate the slowing down of spin fluctuations parallel and perpendicular to the kagome lattice of YCOB, respectively, at $H \parallel c$. However, even in the fully frustrated and disorder-free case, the slowing down of spin fluctuations is also expected in the quantum spin liquid (QSL) phase at low T , as the thermal fluctuations must be dramatically suppressed by cooling. In following paragraphs, we compare the main features of our NMR results measured on YCOB with those of other well-studied QSL candidates.

(1) The spin-lattice relaxation rate of YCOB only slightly increases by less than two times as the temperature decreases from $\sim 300 \text{ K}$ down to 1.7 K (Supplementary Fig. 6a), which suggests the survival of strong quantum fluctuations along the kagome lattice, $\sim 70\%$ of the total spin fluctuations seen at high T [10]. This feature is consistent with the expectation of the gapless (spin gap $< 1.7 \text{ K} \sim 0.03\langle J_1 \rangle$) QSL



Supplementary Figure 6. Temperature evolution of NMR quantities and bulk susceptibilities.

Temperature dependence of spin-lattice relaxation rates ($1/T_1$, **a**), full widths at half maximum (FWHMs) of the main NMR lines (**b**), and spin-spin relaxation rates ($1/T_2$, **c**). The insets of **a-c** present the log-log plots of the corresponding data. In the inset of **a**, the solid line displays the power-law fit, $1/T_1 \sim T^{-0.21(1)}$, whereas the dashed line shows a slowing down of thermal/classical fluctuations, $1/T_1 \sim T^{-1}$, for comparison. **(d)** ac susceptibilities (real parts) measured by applying ac magnetic fields with various frequencies and the fixed amplitude of 1 mT, parallel and perpendicular to the c axis. **(e)** dc susceptibilities measured at 10 mT under zero-field cooling (ZFC) and field cooling (FC), respectively. The data of **d** and **e** are abstracted from ref. [1].

phase either with or without nodes [11]. Upon cooling, the similar increase of low- T $1/T_1$ was also observed in the triangular-lattice QSL candidates $\text{EtMe}_3\text{Sb}[\text{Pd}(\text{dmit})_2]_2$ [11] and $\text{Na}_2\text{BaCo}(\text{PO}_4)_2$ below 2 T [12], the three-dimensional candidate $\text{PbCuTe}_2\text{O}_6$ below ~ 2 K [13], etc.

(2) The FWHMs of the Br1 and Br2 NMR lines increase by ~ 5 and 10 times, respectively, as the temperature decreases from ~ 300 K down to 1.7 K in YCOB (Supplementary Fig. 6b). Similarly, in the well-known kagome-lattice QSL candidate $\text{ZnCu}_3(\text{OH})_6\text{Cl}_2$ FWHMs also increase by ~ 10 times from ~ 120 K down to the lowest temperature [14]. The similar inhomogeneous broadening of NMR lines was also observed in the triangular-lattice QSL candidates $\text{EtMe}_3\text{Sb}[\text{Pd}(\text{dmit})_2]_2$ [11] and $\kappa\text{-(ET)}_2\text{Cu}_2(\text{CN})_3$ [15].

(3) The enhancement of $1/T_2$ (Supplementary Fig. 6c) at low T is also very common among QSL candidates, as reported in refs [13, 15, 16] for instance.

In summary, our NMR results (including $1/T_1$, FWHM, and $1/T_2$) of YCOB are well consistent with the previously reported ac and dc susceptibilities [1, 2, 9] and exhibit the common features of well-studied QSL candidates, and speak against a critical slowing down or critical broadening of conventional spin-glass freezing at least down to 1.7 K. No well-defined critical temperature, such as T_c where $1/T_1$ shows a robust peak, can be abstracted from the NMR quantities vs T plots (see Supplementary Fig. 6a-c).

Supplementary Note 6. Negligible second-order quadrupole shifts of the main NMR lines

Both ^{81}Br and ^{79}Br have large quadrupole moments, but the quadrupole shifts of both Br1 and Br2 main lines are symmetrically forbidden in our NMR measurements on YCOB. Both point groups on Br1 and Br2 positions contain the three-fold rotational symmetry on the c (z) axis R_3^z , and thus the general electric field gradient (EFG) tensor that is invariant under R_3^z is given by

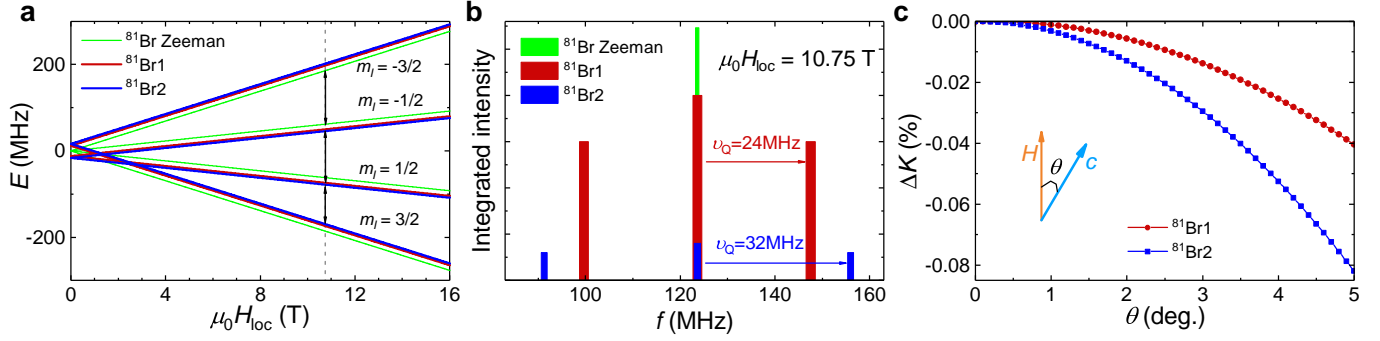
$$\mathbf{V} = \begin{pmatrix} V_{xx} & 0 & 0 \\ 0 & V_{xx} & 0 \\ 0 & 0 & V_{zz} \end{pmatrix}. \quad (3)$$

There are only two parameters V_{xx} and V_{zz} that depend on the distinctive Wyckoff positions, $2d$ (Br1) and $1a$ (Br2). As long as $|V_{zz}| > |V_{xx}|$ is satisfied, the second-order quadrupole shift of the main line is symmetrically forbidden in our experiments. As shown in the main text the measured NMR shifts of Br1 and Br2 lines can be naturally understood by the ab-initio many-body simulation without any quadrupole corrections, and of course this is a strong signature of the absence of profound quadrupole shifts at the main lines.

To clear the doubt away, we conducted the DFT calculation of the EFG tensors at Br1 and Br2 sites by considering the possible misalignment of the crystal and structural disorder. We started with several optimized crystal structures for supercells containing different environments of Br/OH, and then calculated the EFG tensors at various Br1 and Br2 sites. Typical EFG tensors at Br1 and Br2 sites are obtained,

$$\mathbf{V}(\text{Br1}) = \begin{pmatrix} -35.746 & 0.282 & 0.390 \\ 0.282 & -36.057 & 0.283 \\ 0.390 & 0.283 & 71.803 \end{pmatrix}, \mathbf{V}(\text{Br2}) = \begin{pmatrix} -48.510 & 0.029 & 0.080 \\ 0.029 & -48.491 & 0.019 \\ 0.080 & 0.019 & 97.001 \end{pmatrix}, \quad (4)$$

in $\text{V}/\text{\AA}^2$. Obviously, all of the calculated EFG tensors with the quenched structural disorder are very close to the general form presented in Supplementary equation (3) with $|V_{zz}| > |V_{xx}|$.



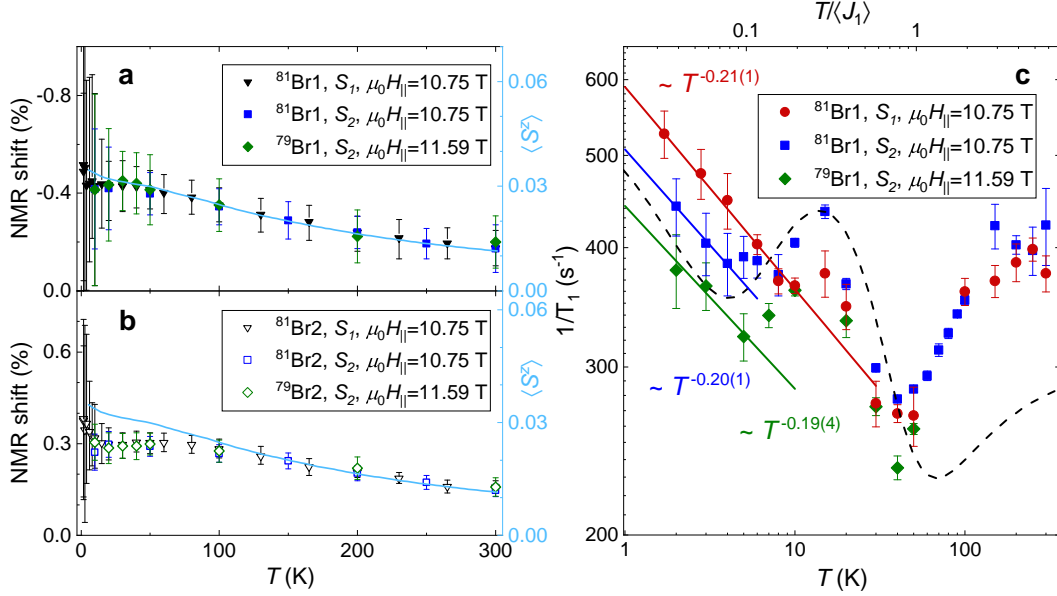
Supplementary Figure 7. Simulations of the quadrupole effects. (a) The field dependence of eigenvalues of Supplementary equation (5) calculated for $\mathbf{V}(\text{Br1})$ and $\mathbf{V}(\text{Br2})$. (b) The NMR spectra at $\mu_0 H_{\text{loc}} = 10.75$ T. Nearly zero quadrupole correction (shift) of the main peak is observed, and two satellite lines are well separated from the main one by the nuclear quadrupole frequency $\nu_Q > 20$ MHz. (c) The misalignment angle (θ) dependence of quadrupole corrections calculated for $\mathbf{V}(\text{Br1})$ and $\mathbf{V}(\text{Br2})$. θ is the possible small angle between the c axis and applied magnetic field, as shown in the inset.

Under the local magnetic field of $\mu_0 H_{\text{loc}}$ applied along the c (z) axis, the total Hamiltonian (in Hz) as the sum of the Zeeman (dipole) and quadrupole terms is given by

$$\mathcal{H}_{\text{NMR}} = -\mu_0 H_{\text{loc}} \gamma_n I_z + \frac{eQ}{2I(2I-1)\hbar} \mathbf{I} \cdot \mathbf{V} \cdot \mathbf{I}^T, \quad (5)$$

where $\mathbf{I} = [I_x, I_y, I_z]$, $I = 3/2$, $\gamma_n = 11.4989$ and 10.6675 MHz/T, $Q = 0.276$ and $0.330 \times 10^{-28} \text{m}^2$, for ^{81}Br and ^{79}Br nuclear spins, respectively. The Hamiltonian of Supplementary equation (5) can be diagonalized exactly, the eigenvalues E_n and integrated intensities proportional to $|\langle E_{n'} | I_x | E_n \rangle|^2$ can be obtained, as shown in Supplementary Fig. 7a,b for $\mathbf{V}(\text{Br1})$ and $\mathbf{V}(\text{Br2})$. The three lines of the NMR spectrum are well separated by the nuclear quadrupole frequency $\nu_Q = \frac{3eQ\tilde{V}_{zz}}{2I(2I-1)\hbar} > 20$ MHz, where \tilde{V}_{zz} is the largest absolute eigenvalue of \mathbf{V} . As a result, we only observed the main Br NMR lines of YCOB in our frequency range (see main text), and the second-order quadrupole shifts of the main lines are essentially negligible even in the presence of the inherent disorder, $|\Delta K| < 10^{-6}$.

We used the high-quality single crystals of YCOB on perfect flaky shape, and mounted the crystal sheets perpendicular to the applied magnetic field, i.e. $c \parallel H$, with carefulness. As a result, we found the misalignment angle (θ) is typically very small based on Laue x-ray diffraction, saying $\theta < 5^\circ$. The rotation



Supplementary Figure 8. Weak sample dependence of NMR shifts and spin-lattice relaxation rates.

Temperature dependence of the main NMR shifts of Br1 (a) and Br2 (b) nuclear spins, with the bulk magnetization ($\langle S^z \rangle$) measured at $\mu_0 H_{\parallel} = 10.75$ T for comparison. The bars display the normalized frequency regions where the intensity is larger than half of the maximum value. (c) Temperature dependence of Br1 nuclear spin-lattice relaxation rates $1/T_1$. The colored lines present the power-law fits to the experimental data below 10 K, and the dashed line shows $1/T_1$ calculated by using the random KHA model of YCOB.

matrix is given by

$$\mathbf{R}(\theta, \varphi) = \begin{pmatrix} \cos \theta + (1 - \cos \theta) \cos^2 \varphi & (1 - \cos \theta) \sin \varphi \cos \varphi & \sin \theta \sin \varphi \\ (1 - \cos \theta) \sin \varphi \cos \varphi & \cos \theta + (1 - \cos \theta) \sin^2 \varphi & -\sin \theta \cos \varphi \\ -\sin \theta \sin \varphi & \sin \theta \cos \varphi & \cos \theta \end{pmatrix}, \quad (6)$$

where $0 \leq \varphi < 360^\circ$. By replacing \mathbf{V} with $\mathbf{R}(\theta, \varphi)^{-1} \cdot \mathbf{V} \cdot \mathbf{R}(\theta, \varphi)$ in Supplementary equation (5), we calculated the quadrupole shift of main line ΔK (see Supplementary Fig. 7c), which is nearly independent of φ due to $\tilde{V}_{yy} \approx \tilde{V}_{xx}$. Even when a misalignment of $\theta < 5^\circ$ is taken into account, the quadrupole shifts of main lines are still negligible, $|\Delta K| < 0.08\%$, much smaller than the measured Knight shifts and line widths. Since the second-order quadrupole shifts of main NMR lines are symmetrically forbidden by R_3^z , the zero shift can act as the reference in our NMR measurements on the single crystal of YCOB with $c \parallel H$.

The Br1 (2d) and Br2 (1a) sites are symmetrically different with profoundly different distances and hyperfine paths to the electronic spin of magnetic Cu^{2+} , $|\text{Br1}-\text{Cu}| = 2.88 \text{ \AA}$ and $|\text{Br2}-\text{Cu}| = 4.49 \text{ \AA}$, which

should account for the observed large difference of the hyperfine couplings, $A_{\text{hf1}} = -0.68(2) \text{ T}/\mu_{\text{B}}$ and $A_{\text{hf2}} = 0.55(3) \text{ T}/\mu_{\text{B}}$ at Br1 and Br2 sites, respectively, in the absence of the second-order quadrupole shifts. It is difficult to reproduce these hyperfine couplings by first-principles calculations, due to the complicated underlying mechanism including both the positive and negative contributions.

As shown by the ab-initio many-body simulations (see the main text) the local spin susceptibilities at Br1 and Br2 sites, $\chi_{\text{loc}}(\text{Br1})$ and $\chi_{\text{loc}}(\text{Br2})$, are distinguishable only at low temperatures ($T < 100 \text{ K}$). However, above $100 \text{ K} > \langle J_1 \rangle$ the spin susceptibilities get nearly homogeneous as evidenced by the minimal widths of the main NMR lines (Supplementary Fig. 6b), the difference between the calculated $\chi_{\text{loc}}(\text{Br1})$ and $\chi_{\text{loc}}(\text{Br2})$ is much smaller than the observed standard deviation of Knight shifts (see Fig. 3a in the main text), and thus the equation $K = A_{\text{hf}}\chi_{\text{loc}} + K_0$ with $\chi_{\text{loc}}(\text{Br1}) \approx \chi_{\text{loc}}(\text{Br2}) \approx \chi_{\text{bulk}}$ holds very well. As a result, we are able to obtain the precise hyperfine couplings of Br1 and Br2 separately, by using the same bulk susceptibility (χ_{bulk}) measured by VSM, above 100 K (see inset of Fig. 2c in the main text).

To test the repeatability of the above results, we performed the independent NMR measurements on another single-crystal sample S_2 ($\sim 15.2 \text{ mg}$) that most likely has a different small misalignment angle θ , but no essential difference from that measured on S_1 was found. The main shifts and $1/T_1$ from both ^{81}Br and ^{79}Br nuclear spins measured on S_2 are shown in Supplementary Fig. 8, with comparison to the ^{81}Br NMR results measured on S_1 . The profiles of the NMR spectra measured at ^{81}Br and ^{79}Br frequencies are highly consistent with each other (see Supplementary Fig. 3), and the different hyperfine couplings measured at Br1 ($A_{\text{hf1}} = -0.68(2) \text{ T}/\mu_{\text{B}}$) and Br2 ($A_{\text{hf2}} = 0.55(3) \text{ T}/\mu_{\text{B}}$) lines are confirmed by the T dependence of both ^{81}Br and ^{79}Br NMR shifts measured on S_2 (see Supplementary Fig. 8a,b).

Supplementary References

-
- [1] J. Liu, L. Yuan, X. Li, B. Li, K. Zhao, H. Liao, and Y. Li, "Gapless spin liquid behavior in a kagome Heisenberg antiferromagnet with randomly distributed hexagons of alternate bonds," *Phys. Rev. B* **105**, 024418 (2022).
 - [2] X.-H. Chen, Y.-X. Huang, Y. Pan, and J.-X. Mi, "Quantum spin liquid candidate $\text{YCu}_3(\text{OH})_6\text{Br}_2[\text{Br}_x(\text{OH})_{1-x}]$ ($x \approx 0.51$): With an almost perfect kagom e layer," *J. Magn. Magn. Mater.* **512**, 167066 (2020).
 - [3] G. C. Carter, L. H. Bennett, and D. J. Kahan, *Metallic shifts in NMR: A review of the theory and comprehensive critical data compilation of metallic materials. Progress in Materials Science* (Pergamon Press, 1976).
 - [4] See <https://www.originlab.com/doc/Origin-Help/Interpret-Regression-Result> for adj. R^2 .
 - [5] A. T. Ogielski, "Dynamics of three-dimensional Ising spin glasses in thermal equilibrium," *Phys. Rev. B* **32**, 7384–7398 (1985).

- [6] M.-H. Julien, F. Borsa, P. Carretta, M. Horvatić, C. Berthier, and C. T. Lin, “Charge segregation, cluster spin glass, and superconductivity in $\text{La}_{1.94}\text{Sr}_{0.06}\text{CuO}_4$,” *Phys. Rev. Lett.* **83**, 604–607 (1999).
- [7] X. Zong, A. Niazi, F. Borsa, X. Ma, and D. C. Johnston, “Structure, magnetization, and NMR studies of the spin-glass compound $(\text{Li}_x\text{V}_{1-x})_3\text{BO}_5$ ($x \approx 0.40$ and 0.33),” *Phys. Rev. B* **76**, 054452 (2007).
- [8] M. Frachet, I. Vinograd, R. Zhou, S. Benhabib, S. Wu, H. Mayaffre, S. Krämer, S. K. Ramakrishna, A. P. Reyes, J. Debray, T. Kurosawa, N. Momono, M. Oda, S. Komiya, S. Ono, M. Horio, J. Chang, C. Proust, D. LeBoeuf, and M.-H. Julien, “Hidden magnetism at the pseudogap critical point of a cuprate superconductor,” *Nat. Phys.* **16**, 1064 (2020).
- [9] Z. Zeng, X. Ma, S. Wu, H.-F. Li, Z. Tao, X. Lu, X.-h. Chen, J.-X. Mi, S.-J. Song, G.-H. Cao, G. Che, K. Li, G. Li, H. Luo, Z. Y. Meng, and S. Li, “Possible Dirac quantum spin liquid in the kagome quantum antiferromagnet $\text{YCu}_3(\text{OH})_6\text{Br}_2[\text{Br}_x(\text{OH})_{1-x}]$,” *Phys. Rev. B* **105**, L121109 (2022).
- [10] Y. Li, D. Adroja, P. K. Biswas, P. J. Baker, Q. Zhang, J. Liu, A. A. Tsirlin, P. Gegenwart, and Q. Zhang, “Muon spin relaxation evidence for the U(1) quantum spin-liquid ground state in the triangular antiferromagnet YbMgGaO_4 ,” *Phys. Rev. Lett.* **117**, 097201 (2016).
- [11] T. Itou, A. Oyamada, S. Maegawa, M. Tamura, and R. Kato, “Quantum spin liquid in the spin-1/2 triangular antiferromagnet $\text{EtMe}_3\text{Sb}[\text{Pd}(\text{dmit})_2]_2$,” *Phys. Rev. B* **77**, 104413 (2008).
- [12] S. Lee, C. H. Lee, A. Berlie, A. D. Hillier, D. T. Adroja, R. Zhong, R. J. Cava, Z. H. Jang, and K.-Y. Choi, “Temporal and field evolution of spin excitations in the disorder-free triangular antiferromagnet $\text{Na}_2\text{BaCo}(\text{PO}_4)_2$,” *Phys. Rev. B* **103**, 024413 (2021).
- [13] P. Khuntia, F. Bert, P. Mendels, B. Koteswararao, A. V. Mahajan, M. Baenitz, F. C. Chou, C. Baines, A. Amato, and Y. Furukawa, “Spin liquid state in the 3D frustrated antiferromagnet $\text{PbCuTe}_2\text{O}_6$: NMR and muon spin relaxation studies,” *Phys. Rev. Lett.* **116**, 107203 (2016).
- [14] M. Fu, T. Imai, T.-H. Han, and Y. S. Lee, “Evidence for a gapped spin-liquid ground state in a kagome Heisenberg antiferromagnet,” *Science* **350**, 655–658 (2015).
- [15] Y. Shimizu, K. Miyagawa, K. Kanoda, M. Maesato, and G. Saito, “Emergence of inhomogeneous moments from spin liquid in the triangular-lattice Mott insulator $\kappa\text{-(ET)}_2\text{Cu}_2(\text{CN})_3$,” *Phys. Rev. B* **73**, 140407 (2006).
- [16] J. A. Quilliam, F. Bert, A. Manseau, C. Darie, C. Guillot-Deudon, C. Payen, C. Baines, A. Amato, and P. Mendels, “Gapless quantum spin liquid ground state in the spin-1 antiferromagnet $6\text{HB-Ba}_3\text{NiSb}_2\text{O}_9$,” *Phys. Rev. B* **93**, 214432 (2016).